

Using mineral chemistry to aid exploration – a case study from the Resolution porphyry Cu-Mo deposit, Arizona

David R. Cooke^{1,2}, Jamie J. Wilkinson^{1,3,4}, Mike Baker^{1,2}, Paul Agnew⁵, Josh Phillips^{1,*}, Zhaoshan Chang^{1#}, Huayong Chen^{1@}, Clara C. Wilkinson^{1,3}, Shaun Inglis¹, Pete Hollings⁶, Lejun Zhang^{1,2}, J. Bruce Gemmell^{1,2}, Noel C. White⁷, Leonid Danyushevsky¹, and Hamish Martin⁸

1 – ARC Research Hub for Transforming the Mining Value Chain, University of Tasmania, Private Bag 79, Hobart, Tasmania 7001, Australia

2 – Centre for Ore Deposit and Earth Sciences (CODES), University of Tasmania, Private Bag 79, Hobart, Tasmania 7001, Australia

3 – Department of Earth Sciences, Natural History Museum, Cromwell Road, London SW7 5BD, United Kingdom

4 – Department of Earth Science and Engineering, Imperial College London, Exhibition Road, London SW7 2AZ, United Kingdom

5 – Rio Tinto Exploration, Research Avenue, Bundoora, Victoria 3083, Australia

6 – Department of Geology, Lakehead University, Thunder Bay, Ontario P7B 5E1, Canada

7 - Ore Deposit and Exploration Centre (ODEC), School of Resources and Environmental Engineering, Hefei University of Technology, Hefei, Anhui 230009, China

8 – Resolution Copper Mining, P.O. Box 1944, Superior, Arizona 85173, USA

** – Current address: Freeport McMoRan Exploration Australasia, Level 4, 80 Petrie Terrace, Brisbane, Queensland 4000, Australia*

– Current address: Department of Geology and Geological Engineering, Colorado School of Mines, Golden, Colorado 80401, USA

@ - Current address: Key Laboratory of Mineralogy and Metallogeny, Guangzhou Institute of Geochemistry, Chinese Academy of Sciences, Guangzhou, Guangdong 510640, China

Abstract

The giant, high-grade Resolution porphyry Cu-Mo deposit in the Superior District of Arizona is hosted in Proterozoic and Paleozoic basement, and in an overlying Cretaceous volcanoclastic breccia and sandstone package. Resolution has a central domain of potassic alteration that extends more than 1 km outboard of the ore zone, overlapping with a propylitic halo characterized by epidote, chlorite and pyrite that is particularly well developed in the Laramide volcanoclastic rocks and Proterozoic dolerite sills. The potassic and propylitic assemblages were overprinted in the upper parts of the deposit by intense phyllic and advanced argillic alteration. The district was disrupted by Tertiary Basin and Range extension, and the fault block containing Resolution and its Cretaceous host succession was buried under thick mid-Miocene dacitic volcanic cover, obscuring the geological, geophysical and geochemical footprint of the deposit.

To test the potential of propylitic mineral chemistry analyses to aid in the detection of concealed porphyry deposits, a blind test was conducted using a suite of epidote–chlorite ± pyrite-altered Laramide volcanoclastic rocks and Proterozoic dolerites collected from the propylitic halo, with samples taken from two domains located to the north and south and above the Resolution ore zone. LA-ICP-MS data of epidote provided indications of deposit fertility and proximity. Competition for chalcophile elements (As, Sb, Pb) between coexisting pyrite and epidote grains led to a subdued As-Sb fertility response in epidote, consistent with epidote collected between 0.7 and 1.5 km from the center of a large porphyry deposit. Temperature-sensitive trace elements in chlorite provided coherent spatial zonation patterns implying a heat source centered at depth between the two sample clusters, and application of chlorite proximator calculations based on LA-ICP-MS analyses provided a precisely defined drill target in this location in three dimensions. Drilling of this target would have resulted in

the discovery of Resolution, confirming that epidote and chlorite mineral chemistry can potentially add value to porphyry exploration under cover.

Introduction

Human civilization produced as much copper over the past 25 years (1993–2018) as it did over the entire previous history of industrial activity (Pietrzyk and Tora, 2018; USGS, 2019). With significant growth in global population, technological advancement, urbanization, and copper's growing importance as a green metal for renewable energy solutions, society's demand for this metal increases annually. This creates a strong imperative for mineral exploration to deliver new copper resources.

Most of the world's copper, together with significant gold and molybdenum, is recovered from porphyry ore deposits, making them one of the most sought-after ore deposit types (Sillitoe, 2010). With maturing exploration in the world's major porphyry copper provinces (e.g., Chile, Arizona, Papua New Guinea), porphyry exploration has been transitioning from the quest for outcropping or near-surface (open pit) ores to more deeply buried resources. This presents considerable challenges to exploration and requires significant innovation (Holliday and Cooke, 2007). There have been several significant success stories of porphyry discoveries under cover in the past three decades, including Ridgeway (New South Wales), Pebble East (Alaska), Cukaru Peki (Serbia), Hugo Dummett (Mongolia), Pampa Escondida (Chile) and Resolution (Arizona). These are mostly brownfields discoveries, with deep drilling and geological vectoring essential parts of the discovery process. Deep-penetrating geophysical surveys have also strongly impacted on porphyry exploration in the new millennium (Holliday and Cooke, 2007); however, geochemical exploration has lagged due to the challenges of detecting low-level geochemical anomalies through post-

mineralization cover or in the most distal parts of the propylitic alteration halos that surround porphyry deposits (Cooke et al., 2020).

Significant efforts have been devoted over the past two decades to mineral chemistry investigations to help improve the impact of geochemical exploration on porphyry deposit discoveries (Cooke et al., 2020). Research into porphyry indicator minerals aims to identify the presence of, or potential for, porphyry-style mineralization based on the chemistry of igneous minerals such as zircon (Ballard et al., 2002; Dilles et al., 2015; Loader et al., 2017); apatite (Mao et al., 2016), plagioclase (Williamson et al., 2016; Cao et al., this volume), or resistate hydrothermal minerals such as magnetite (Cross, 2000; Dupuis and Beaudoin, 2011; Nadoll et al., 2015). Research into porphyry vectoring and fertility tools aims to use the chemical compositions and related spectral characteristics of hydrothermal minerals such as epidote, chlorite and alunite to predict the likely direction and distance to mineralized centers, and the potential metal endowment of a mineral district (e.g., Chang et al., 2011; Cooke et al., 2014; Wilkinson et al., 2015; Neal et al., 2018; Uribe-Mogollon and Maher, 2018; Baker et al., this volume; Wilkinson et al., this volume; Pacey et al., this volume a and b, Ahmed et al., this volume; Alva-Jimenez et al., this volume; Byrne et al., this volume). This new generation of exploration tools has been enabled by advances in laser ablation inductively coupled plasma mass spectrometry (LA-ICP-MS), short wave infrared (SWIR) data acquisition and data processing, and the increased availability of microanalytical techniques such as cathodoluminescence imaging.

This article presents a case study of a blind test of epidote and chlorite mineral chemistry from the giant Resolution porphyry Cu-Mo deposit of the Superior district of Arizona (Fig. 1). We demonstrate how the analysis of subtle, low-level hypogene geochemical signals preserved in distal propylitic alteration minerals around porphyry deposits can potentially aid exploration for porphyry deposits under cover. To achieve this aim, we also present the

results of petrographic, whole rock geochemical, SWIR and K-feldspar staining results to highlight the effectiveness of combining datasets in aiding the detection of concealed, porphyry-style mineralization.

Blind testing – Rationale

The results presented below were generated as part of a blind test conducted by researchers in the AMIRA International research project P765A – “Transitions and zoning in porphyry and epithermal districts”. The concept of blind testing was first introduced to the AMIRA footprints research program (2004–2021) as part of AMIRA P765A in early 2008. It was instigated as a way for industry to test and validate new geochemical and geological exploration tools being developed by the research team. A blind test involved an industry sponsor providing the research team with a suite of samples from a traverse, grid or cross-section from a district that contains a known mineral resource. The location and identity of the district and deposit remain concealed from the research team for the duration of the test, but the researchers were provided with a set of relocated but internally consistent sample coordinates (including elevation) so that the spatial relationships between samples are not compromised. The research team were also provided with sample metadata and whole rock geochemical data for each sample. These data were used to assess whether mineral chemistry provides additional insights for exploration beyond those gained by conventional multi-element whole rock analyses of the rock chips. Operating within these protocols, blind testing facilitated the refinement of new tools for exploration in districts where the industry sponsors know that a significant mineral resource exists, or where a false positive may be detected. Sponsors are required to reveal the location of the blind test only after the research team has completed the test through the presentation of their results and interpretations at a sponsors’ research meeting.

Blind tests in the green rock environment should ideally involve a suite of approximately 30 samples collected from a grid with a sample spacing of approximately 300 to 500 m. These protocols could not be followed in the Resolution blind test due to the constraints of drill hole coverage. Instead, a total of 12 samples were provided on an approximate N-S cross-section, with samples clustered in two domains, separated by approximately 2 km (Fig. 1). Rio Tinto Exploration, who provided the sample suite, also provided the following context at the start of the blind test: *“The sample geometry is terrible... however, this is the real world so let me put these samples in context. Pretend we are drilling a deep porphyry target under cover. Holes are deep and expensive. Pretend that to date we have been unsuccessful and hit nothing other than propylitic alteration and a hint of pyrite. We can probably work out a vector from the pyrite for the next hole. But the big question is, with management fatigue setting in, should we bother? Does the chlorite and / or epidote chemistry suggest we have a fertile system nearby? How do the numbers compare to other systems studied by the AMIRA team? Could it be a high-grade system? Are we close? Most likely direction? Is there a thermal gradient evident in chlorite? These samples are from a known system, so we will be able to make a genuine assessment of the toolbox performance.”* – Paul Agnew, Rio Tinto Exploration, personal communication, February 2009”.

Superior District – geology and mineralization

Arizona is well-endowed with giant Laramide porphyry Cu-Mo deposits. The Superior District is one of the many highly mineralized Cretaceous to Paleocene porphyry districts in the region. In addition to Resolution, the district contains the Superior East porphyry Cu-Mo deposit (Sell, 1995), high-grade epithermal Cu-Ag veins and mantos at Magma (Gustafson, 1961), breccia-hosted epithermal Ag mineralization at Silver King, and several other epithermal vein and manto prospects (Fig. 2).

The Superior District is underlain by the Paleoproterozoic (~1,650 Ma) Pinal Schist (Fig. 2), a package of quartz-muscovite and quartz-chlorite schists with minor intercalations of calc-silicate and metavolcanic rocks, and a dominant NE-trending foliation (Condie and De Melas, 1985; Eisele and Isachsen, 2001). Meta-turbidites of the Pinal Schist are overlain unconformably by shallow marine to locally evaporitic Mesoproterozoic sedimentary and mafic volcanic rocks of the Apache Group (Fig. 3), which are well-exposed in the lower parts of the range front of the Dripping Springs Mountains, to the west of Resolution (Fig. 2). Apache Group sedimentation and volcanism commenced with the deposition of the Pioneer Shale, and continued with the Drippings Springs Quartzite, Mescal Limestone and Apache Basalt (Short et al., 1943; Shride, 1967; McConnell, 1975; Wrucke, 1989). These units are overlain by the Mesoproterozoic Troy Quartzite, which is interpreted to be syn-orogenic detritus derived from the Grenville Orogen (Mulder et al., 2017).

Extensive mafic magmatism affected the Superior District and the broader region during the Mesoproterozoic, with the emplacement of a series of dolerite sills into the Apache Group sedimentary rocks (Figs. 2 and 3). The dolerites are composed chiefly of fine- to coarse-grained plagioclase and pyroxene with ophitic to sub-ophitic textures (Figs. 4A-D). U-Pb dating of zircon and baddeleyite by Bright et al. (2014) constrained dolerite emplacement between 1,110 and 1,075 Ma, coeval with the development of the North American Midcontinent Rift, which is host to Ni-Cu-PGE mineralization (Heaman et al., 2007; Miller et al., 2013).

A sequence of Paleozoic carbonates and quartzites unconformably overlie the Mesoproterozoic and Paleoproterozoic rocks of the Superior District (Fig. 3). The Cambrian Bolsa Quartzite, and limestones of the Devonian Martin Formation, Mississippian Escabrosa Limestone and Pennsylvanian Naco Formation are well-exposed at progressively higher elevations in the Range Front (Fig. 2; Short et al., 1943; Friehauf and Pareja, 1998; Schwarz, 2007) and provide evidence for a protracted history of shallow marine sedimentation in the

Paleozoic. The Paleozoic carbonate rocks are important hosts to manto-style carbonate replacement mineralization at Magma (Paul and Knight, 1995; Frieauf, 1998; Frieauf and Pareja, 1998) and also host high-grade skarn mineralization at Resolution (McCarrel, 2012; Hehnke et al., 2012).

Cretaceous rocks are poorly exposed in the Superior District. A Late Cretaceous quartz diorite stock and dacite porphyry crops out at the Silver King mine to the northwest of the Magma Mine (Fig. 2). An unexposed sequence of Late Cretaceous to Early Tertiary andesitic to dacitic volcanoclastic and pyroclastic rocks occupy a half-graben to the east of the Range Front—this package hosts the upper part of Resolution (Fig. 5; Schott, 1994) and was not known until intersected by underground drilling from Magma in 1959 (Hammer, pers. commun., 2011; Phillips, 2019). The basal quartzose sandstone is overlain by a thick package of volcanic sandstones and breccias (Fig. 6) that are mostly andesitic to rhyodacitic in composition. Late-stage latite to rhyolite porphyry dikes cut the volcanoclastic sequence.

The range front to the east of Superior exposes a thick package of Middle to Late Tertiary volcanic rocks that unconformably overlie the Proterozoic, Paleozoic and Cretaceous sequences and completely obscure the presence of Resolution (Figs. 2 and 5). The sequence consists of the basal Whitetail Conglomerate (locally > 1.5 km thick), Haunted Canyon Volcanics, Apache Leap Tuff (~500 m thick; Fig. 5), Tertiary basalt and the Gila Conglomerate (Hehnke et al., 2012; Phillips, 2019). The Apache Leap Tuff defines most of the volcanic plateau that crops out to the east of Superior (Fig. 2).

Middle to Late Tertiary Basin and Range extension disrupted the Superior District significantly and influenced Tertiary volcanism and sedimentation (Fig. 2). Deposition of the Whitetail Conglomerate was localized within a half-graben by the Devils Canyon Fault. This major extensional fault is inferred to have facilitated block rotation during Tertiary Basin and Range extension, resulting in almost 2 km of down-to-the-west displacement that caused the

fault block hosting Resolution to rotate approximately 25° ENE post-mineralization (Hehnke et al., 2012). North- to NW-trending normal faults further disrupted the Superior District in the Tertiary and Quaternary (Fig. 2). The Concentrator Fault, which bounds the western side of the Range Front (Fig. 1), is inferred to have a vertical displacement of almost 1.3 km (Phillips, 2019).

Resolution porphyry Cu-Mo deposit

The giant, high-grade Resolution porphyry Cu-Mo deposit is located five kilometers east of Superior, Arizona, USA (Fig. 2). It was discovered by Magma Copper Co. and BHP Billiton via underground and surface drilling in an exploration campaign that ran from 1994 to 1998 (Manske and Paul, 2002). Between 2001 and 2003, Kennecott Exploration Co. delineated the porphyry resource at a depth of more than 1,300 m below surface. The project is now managed by Resolution Copper Mining LLC, and is owned 55 per cent by Resolution Copper Company and 45 per cent by BHP Copper Inc. Although its size has not been fully defined, the deposit is characterized by consistent grades of > 1% Cu mineralization above an elevation of 750 m below sea level, in suitable host rocks (e.g., highly reactive dolerites and limestones, and permeable breccias). The orebody extends at least 2 km in an ENE direction and 1.5 km in a north-northwest direction (Fig. 2) and is locally greater than 500 m thick (Fig. 5). Significant, but lower-grade mineralization extends beyond this defined body of strong mineralization. The total inferred resource is 1.787 billion tonnes at a grade of 1.53% Cu and 0.039% Mo (Rio Tinto Annual Report, 2018).

Resolution had a protracted and productive history of hydrothermal activity (Schwartz, 2010). A central domain of intense, pervasive to incipient potassic alteration was estimated by Hehnke et al. (2012) to have affected an area of 5 km² (2 x 2.5 x 1 km) between the northern and southern half-graben-bounding faults. Biotite is the dominant potassic alteration mineral in mafic rock units (Schwartz, 2010) but hydrothermal K-feldspar is abundant in

more felsic rock types (Hehnke et al., 2012). Chalcopyrite was the dominant copper sulfide precipitated during potassic alteration.

The potassic core of the deposit is surrounded by an extensive domain of propylitic alteration (the 'green rock environment'; Cooke et al., 2014) dominated by epidote and chlorite that was preferentially developed in the mafic to felsic volcanic, volcanoclastic and intrusive rocks (Phillips, 2019). The pyrite halo to the Resolution deposit extends beyond the potassic core into the propylitic halo, with sulfide abundances increasing strongly inwards towards the deposit center (Hehnke et al., 2012).

A late stage phyllic (quartz–sericite–pyrite) alteration assemblage has overprinted deep-seated potassic and peripheral propylitic-altered rocks and extends for hundreds of meters upwards above the ore zone through the Cretaceous volcanic sandstones and breccias (Hehnke et al., 2012). Within the ore zone, phyllic alteration is characterized by a chalcopyrite–bornite–pyrite assemblage that caused hypogene upgrading of the early chalcopyrite mineralization associated with the potassic zone (Schwartz, 2010). Advanced argillic alteration overprinted the phyllic assemblage at the top of the Resolution orebody, producing dickite, kaolinite, topaz, alunite, zunyite, woodhouseite and pyrophyllite, together with 10%–20% pyrite (Troutman, 2001; Winant, 2010; Hehnke et al., 2012). A late-stage, high sulfidation-state mineral assemblage of bornite–chalcocite–digenite–pyrite associated with sericite–kaolinite caused further hypogene upgrading of the Resolution ore zone (Hehnke et al., 2012). The productivity of early- and late-stage hydrothermal activity at Resolution was a major contributing factor to the size and grade of the hypogene resource (Schwartz, 2010).

Mineralization at Resolution is strongly protolith-dependent, with the best copper grades developed in reactive rocks (limestone, dolerite, volcanoclastic breccia) and lower grades in

non- to weakly-reactive rock types (quartzite, quartzose sandstone, felsic intrusions; Hehnke et al., 2012). Within the ore zone, defined by the 1% Cu shell, chalcopyrite is the dominant copper sulfide (~65%). Although Cu and Mo are well-correlated at the deposit scale, they typically decouple at the outcrop scale (Hehnke et al., 2012), with molybdenite occurring primarily on the margins of straight-sided quartz veins (“B” veins of Gustafson and Hunt, 1975). Molybdenite has an average grade of 370 ppm within the ore zone (Hehnke et al., 2012).

Methods

Rio Tinto Exploration submitted 12 drill core samples of propylitic-altered Cretaceous volcanoclastic rocks and Proterozoic dolerite to AMIRA project P765A as a blind test of the green rock mineral chemistry techniques. These samples were provided with internally consistent sample coordinates, but the actual coordinates were changed by Rio Tinto Exploration systematically for the blind test to obscure the location of the ore deposit. Seven samples came from one deep drill hole (RT006), whereas the remaining five samples came from a cluster of drill holes ~2 km south of RT006 (Fig. 1). Tables 1 and 2 report the real-world UTM coordinates and drill hole information for all 12 samples. Sample locations are plotted on Figures 1 and 2.

Sample splits were submitted for whole rock geochemical analysis by Rio Tinto Exploration to ACME Analytical Laboratories Ltd. in Vancouver, Canada. Samples were jaw crushed to 70% passing 10 mesh (2 mm), a 250 g aliquot was riffle split and pulverized to 95% passing 150 mesh (100 μm) in a mild-steel, ring-and-puck mill. 0.2 g of powdered sample were fused in a graphite crucible with 1.5 g of $\text{LiBO}_2/\text{LiB}_4\text{O}_7$ flux at 980°C for 30 minutes and then dissolved in 5% HNO_3 . Major elements were determined using a Jarrel Ash AtomComp Model 975/Spectro Ciros Vision inductively coupled plasma emission spectrograph and are reported in Table 1. Trace elements were analyzed using a Perkin-Elmer

Elan 6000 or 9000 inductively coupled plasma mass spectrometer and are reported in Table 2 and Digital Appendix A1. For both major and trace elements, calibration standards, verification standards and reagent blanks were included in the sample sequence. Reported detection limits for the major elements are < 0.04 weight percent and < 0.5 ppm for most of the trace elements but < 0.05 ppm for REE.

Polished drill core slabs and 2.54 cm diameter laser mounts were analyzed at the University of Tasmania using a combination of thin section petrography, SWIR, and K-feldspar staining—results are reported in Table 3. The drill core slabs were polished to highlight mineralogical and textural features. The unpolished back side of each slab was etched with hydrofluoric acid and treated with sodium cobaltinitrite using the feldspar staining method of Bailey and Stevens (1960) to detect whether K-feldspar alteration had affected any of the samples (Figs. 4 and 6).

SWIR analyses were collected using the CODES PIMA-II instrument, following the protocols outlined in Chang and Yang (2012). The bandwidth of the PIMA-II is approximately 7 nm and the spectral sampling interval is 2 nm; spectral resolution in the SWIR is closer to 8 nm. Two to six spots were analyzed from each sample (Table 3).

LA-ICP-MS analyses of epidote, chlorite and pyrite grains were conducted at CODES Analytical Laboratories, University of Tasmania. LA-ICP-MS analytical methodologies for epidote are provided in Cooke et al. (2014) and Ahmed et al. (this volume). The chlorite analytical method used is from Wilkinson et al. (2015) and pyrite from Large et al. (2009); also see Wilkinson et al. (this volume). We obtained 58 valid LA-ICP-MS analyses of pyrite from seven samples (Table 4), 168 valid LA-ICP-MS epidote analyses from 12 samples (Table 5), and 82 valid LA-ICP-MS analyses of chlorite from ten samples (Table 6), together with three epidote, one chlorite and four pyrite LA-ICP-MS maps. When conducting spot analyses, multiple spots were obtained from single grains if the grains were large enough.

Edges of grains were avoided so as to ensure no contamination of the analyses occurred due to accidental ablation of adjacent minerals. Full analytical results are provided in Digital Appendices A2-4 and B1-2.

Results

Geology

Most of the samples analyzed are polymict lithic volcanoclastic breccias and sandstones, characterized by rounded feldspar-hornblende-pyritic andesite, dacite and rare hematitic mudstone clasts in a crystal-rich, mud- to sand-sized matrix (Figs. 4 and 6). Two of the samples are dolerites (Figs. 4A-D).

Each sample contained hand-specimen and petrographic evidence of weak to intense, selectively pervasive propylitic alteration, where epidote has partially to totally replaced plagioclase, hornblende and/or lithic clasts, and chlorite has altered the matrix (Figs. 4 and 6). Epidote occurs as an alteration mineral in all 12 samples and a discontinuous vein of epidote was present in one sample (Fig. 6E).

Pyrite was observed petrographically as an alteration mineral in nine samples, with four of those samples also containing pyrite in quartz veins with pyrite-muscovite alteration halos that also have a late-stage halloysite overprint, mostly from the bottom of drill hole RT006 (Fig. 7A). The presence of pyrite veins correlates with increasing total sulfur concentrations in the whole rock geochemical analyses, which increase from < 0.01 to 2.55 wt % with increasing depth in RT006 (Fig. 7A; Table 1). Chalcopyrite was observed as an alteration mineral in the five deepest samples of RT006, and in one sample from the southern sample cluster. Chalcopyrite was also present as vein fill in four samples from the bottom of RT006, coinciding with Cu concentrations > 0.1 wt % (Fig. 7B; Table 2). At higher elevations, Cu contents were mostly below 100 ppm, consistent with the sparse occurrence of chalcopyrite (Fig. 7B).

K-feldspar staining revealed that most samples have undergone moderate to intense K-feldspar alteration (Figs. 4 and 6), which was not recognized from initial hand-specimen observations. Hydrothermal biotite was observed in two of the deepest samples from RT006 (Figs. 6C and K).

SWIR

SWIR spot analyses confirmed the visual observations of chlorite in all samples and epidote in most samples (Table 3). Epidote was not detected in some of the darker samples, despite its obvious presence, due to limitations of the PIMA instrument operating under low reflectance conditions. Conversely, because of a strong hyperspectral response, montmorillonite was reported from five samples even though it was only observed as a weak dusting of K-feldspar petrographically.

The wavelengths of the ALOH absorption features of white micas near 2,200 nm are related to their octahedral Al (Al^{vi}) contents (Post and Noble, 1993). These Al^{vi} variations are accompanied by changes in Fe and Mg in the white micas due to substitutions (Scott and Yang, 1997; Yang et al., 2011). Following Pontual (2010), we interpret phyllosilicates with ALOH wavelengths of 2,200 to 2,210 nm as muscovite, and wavelengths of 2,216 to 2,228 nm (lower Al^{vi} contents) as phengite. Intermediate wavelengths between 2,210 and 2,216 nm may represent either mixture of muscovite and phengite or micas with intermediate compositions. ALOH wavelengths in the 2,180 to 2,190 nm range are characteristic of paragonite and high Al contents but were not found at the Resolution blind test samples. The 2,200 nm wavelength feature varied across the sample suite from 2,198 to 2,216 nm (Fig. 7C, Table 3), with most of the data between 2,205 and 2,212 nm, suggesting predominantly muscovite compositions. Some values > 2,210 nm were detected, but they have an erratic distribution on the section (Fig. 7C). Muscovite was detected in each sample from drill hole RT006, and in three of the southern samples. The 2,250 nm feature (which relates to chlorite and/or epidote)

ranges from 2,247 to 2,259 nm (Table 3) and has a more consistent spatial distribution, with higher values at higher elevations in the south (Fig. 7D). Surprisingly, halloysite was detected in the two deepest samples from RT006 (Table 3), where it occurs as a weak dusting on the muscovite alteration halos to quartz-pyrite veins (Figs. 6I and K).

Whole rock geochemistry

Tables 1 and 2 summarize whole rock geochemical data from the 12 blind test samples. Despite being classified petrographically either as dolerites or as andesitic to dacitic volcanoclastic breccias and tuffs, several of the samples have geochemical compositions that plot in the fields of alkalic rocks on Figure 8A. On immobile element classification diagrams the samples are sub-alkaline, with predominantly basaltic to andesitic compositions (Fig. 8B), suggesting that the alkali signature relates to K₂O addition during moderate to intense K-feldspar alteration (K₂O up to 7.49 wt %; Table 1). In addition to K-feldspar alteration, most of the samples have been affected by moderate to intense epidote–chlorite alteration (Figs. 4 and 6), and some have been affected by pyrite-muscovite and late-stage halloysite alteration (Figs. 6I and K). Epidote–chlorite alteration has caused significant volatile addition in some samples (loss on ignition values of up to 8.8 wt %; Table 1). Most of the LOI-rich samples still plot as least-altered basalts, andesites and dacites on the alteration box plot of Large et al. (2001), although pyrite–muscovite alteration produces greater Alteration Index values in some samples (Fig. 8C). Similarly, many samples plot close to primary igneous rock compositions on the K/Al vs Na/Al plot despite moderate to strong epidote-chlorite alteration (Fig. 8D). Two samples from the bottom of RT006 that contain quartz-pyrite veins with muscovite vein halos plot near end-member muscovite (Fig. 8D). Three samples that contain both intense K-feldspar and epidote-chlorite alteration have K/Al values around 0.5 and very low Na/Al values, intermediate between the K-feldspar and epidote end-members (Fig. 8D), which is consistent with their observed alteration assemblages.

The geochemical composition of each sample for major and some trace elements is controlled partly by the protolith, and partly by the nature and intensity of metasomatic activity. K₂O contents increase with depth in RT006 (Fig. 9A), consistent with increasing intensity of potassic alteration. Conversely, CaO, TiO₂ and Ni are all impacted by the protolith composition, with high values associated with the two dolerite samples and a basaltic andesite (the southernmost samples and a shallow northern sample on Figs. 9B-D, respectively). Other components enriched in the dolerite include Fe₂O₃, MgO, P₂O₅, Co, Cr, and Sc, whereas SiO₂ is depleted relative to other rock types (Tables 1 and 2).

Pathfinder element compositions in porphyry deposits are typically controlled by the hydrothermal fluids (Halley et al., 2015), unless the local protolith is anomalously enriched in specific trace elements. Several of the trace elements that are considered to be proximal pathfinders (e.g., Emmons, 1927; Halley et al., 2015) increase in abundance with depth at Resolution, including Cu (1.48–3,490 ppm; Figs. 7B and 10A), Te (BDL–3.61 ppm; Fig. 10B), S (BDL–2.55 wt %; Fig. 7A), and also Au (BDL–27.2 ppb), Bi (BDL–7.32 ppm), Se (BDL–1.4 ppm), Sn (BDL–10 ppm) and W (BDL–79.0 ppm; Table 2). Molybdenum is normally a useful proximal pathfinder in porphyry deposits (e.g., Rinne et al., 2018), but for the Resolution blind test sample suite, Mo has a subdued range from 0.18 to 0.69 ppm and shows no significant spatial variations (Table 2).

Trace elements that are considered distal pathfinder elements by Emmons (1927), Chaffee (1982a and b) and Halley et al. (2015) are typically enriched at shallower elevations in the Resolution blind test samples suite (e.g., Mn: 618–3,514 ppm; Zn: 74.5–4,094 ppm; Sb: 0.05–1.45 ppm; Figs. 10D-F), and also Pb (3.64–531.9 ppm) and As (0.3–4.4 ppm; Table 2). Both Zn and Pb are anomalously enriched in the shallowest sample from the southern sample cluster (4.094 ppm Zn and 531.9 ppm Pb; Table 2; Fig. 10E). Lithium tends to be enriched in sericitic alteration above porphyry deposits (Chaffee, 1982a and b; Halley et al., 2015). The

blind test samples show subtle increases in lithium with elevation in RT006 (6.7–16.4 ppm; Fig. 10C; Table 2).

Pyrite chemistry

A total of 58 LA-ICP-MS spot analyses of pyrite were obtained from seven samples (Table 4; Digital Appendix A2), along with four LA-ICP-MS maps that highlight pyrite trace element deportment (Figs. 11 and 12; Digital Appendix B1). There is considerable variability in the concentrations of individual trace elements within and between grains, but overall the most abundant trace elements substituted into the pyrite crystal lattice are Co and Ni, with concentrations typically in the ranges of tens to thousands of ppm (Table 4; Figs. 11 and 12). Other elements present in elevated concentrations in the pyrite crystal lattice include As, Se, Cu, Pb, Te, Zn and Sb. Low concentrations of Ag, Bi, Sn, Au, and Tl (< 1 to 10 ppm) were also detectable in many spot analyses and laser maps (Table 4, Figs. 11 and 12). Silicate and oxide inclusions locally contributed to high concentrations of Mg, Al, Mn, and Ti within individual pyrite grains, and small inclusions of Ag-rich sphalerite and a Bi-telluride were detected during single spot analyses of two pyrite grains (Digital Appendix B1). Growth zones are well-defined by Co, Ni and As in the pyrite cube shown in Figure 11, with Au, Ag, Cu, Bi, Pb and Te relatively enriched in the Co-As-rich core and depleted in the Ni-rich rim.

LA-ICP-MS spot analyses were conducted on cores and rims of four pyrite samples from the deep northern groups of samples (e.g., Fig. 12), and three from the southern domain (e.g., Fig. 11). Overall, pyrite grains from the southern domain are enriched in Sn, Mn, As, Pb, Sb, Ni, Cu, Zn, Ag, Au and Tl relative to the deep northern pyrite grains, which are relatively enriched in Co and Se (Fig. 13; Table 4; Digital Appendix A2).

Epidote chemistry

LA-ICP-MS spot analyses of epidote yielded 168 valid analyses from twelve samples (Table 5; Digital Appendix A3). Additionally, three LA-ICP-MS maps were generated to

illustrate trace element deportment in epidote (Digital Appendix B2). Significant concentrations (10s to 1,000s ppm) of trace elements were determined in epidote from Resolution, including Mn, Sr, Mg, Ti, and V (Table 5), consistent with analyses from other porphyry deposits (Cooke et al., 2014; Ahmed et al., this volume; Baker et al., this volume; Pacey et al., this volume a; Wilkinson et al., this volume). Important distal pathfinder elements in whole rock that substitute into epidote with concentrations typically in the range of 10–100 ppm include As, Sb, Pb, Zn and Mn. Proximal pathfinder elements in whole rock such as Au, Cu, Mo and Sn mostly have concentrations in epidote below the detection limits of the LA-ICP-MS (Table 5; Figs. 13-14). Other trace elements in epidote from Resolution that were commonly detected with concentrations of 1–100s ppm include K, Na, LREE and Zr (Table 5; Digital Appendix A3). When considered spatially, epidote from the shallowest samples in the northern drill hole RT006 are enriched in distal pathfinder elements such as Mn, As and Pb relative to epidote samples from the southern sample cluster and the deeper parts of drill hole RT006 (Figs. 13 E, J and K).

Chlorite chemistry

A total of 82 valid LA-ICP-MS spot analyses of chlorite were obtained from ten samples (Table 6; Digital Appendix A4), along with one LA-ICP-MS map (Digital Appendix B3). Although the composition of chlorite is dominated by Fe, Si, Al and Mg, several trace elements are present in high concentrations (i.e., 10s to 1,000s of ppm) in the Resolution samples, specifically Mn, Zn, V, Ti, Ca, K, Li, Ga, Co, Cr, Na and Ni (Table 6). These results are consistent with the findings from the Batu Hijau porphyry Cu-Au deposit, Indonesia (Wilkinson et al., 2015) and from El Teniente, Chile (Wilkinson et al., this volume). Other trace elements that were typically detected at concentrations < 10 ppm and/or were primarily below detection limits at Resolution include Ag, As, B, Ba, Ce, Cu, La, Pb, Sn, Sr, U, Y, and Zr (Table 6). Laser mapping of a chlorite grain revealed homogenous trace element

distributions (Digital Appendix B3), in contrast to the significant intragrain variability of some of the trace elements hosted in pyrite and epidote (Figs. 11, 12 and Digital Appendix B2).

There are strong spatial controls on the trace element composition of chlorite at Resolution. Titanium contents increase with increasing depth (Fig. 15A), whereas the concentrations of Li, Sr, Pb and Co decrease with increasing depth (Fig. 15B-E). Wilkinson et al. (2015) proposed a series of trace element ‘proximitor’ ratios for chlorite from the Batu Hijau deposit, Indonesia, where the concentrations of trace elements that decrease systematically with distance from the porphyry deposit are divided by those that increase systematically with distance, reducing the signal-to-noise ratio in the trace element data and providing a proxy for distance to deposit center. Figure 15G-J show four chlorite proximitor ratios for Resolution (Ti/Sr, Ti/Li, Ti/Co, Ti/Mn). All four ratios increase systematically with depth in the Resolution sample suite.

Discussion

The purpose of this blind test was to determine if the presence and potential significance of a concealed porphyry deposit could be detected from a limited, unevenly distributed sample suite of propylitic-altered rocks. As the blind test was conducted without the knowledge that the sample suite was collected peripheral to Resolution, this discussion addresses the outcomes of the geological, SWIR, whole rock and mineral geochemistry analyses on propylitic-altered rocks of unknown provenance from the perspective of identifying whether they were collected proximal to a giant, high-grade porphyry Cu-Mo deposit. This allows us to demonstrate whether mineral chemistry can potentially add value to exploration in the green rock environment.

The pyrite halo to most porphyry deposits extends laterally from the potassic-altered core of the deposit outward 1–2 km from the deposit thermal center and defines an inner zone in the broader propylitic halo (Holliday and Cooke, 2007; Cooke et al., 2014, 2020). Pyrite and chalcopyrite were observed as vein-fill and/or alteration minerals in many of the propylitically-altered blind test samples, implying that they could come from the inner, pyrite-bearing, propylitic alteration halo to a porphyry deposit. Four of the samples contained chalcopyrite-bearing veins, mostly from the bottom of RT006, where anomalous Cu (up to 0.35%) and S (up to 2.6%) were detected (Figs. 7A-B and 10A). These features are consistent with increasing proximity to a porphyry deposit center at depth.

The results of K-feldspar staining (Figs. 4 and 6) highlighted a widespread spatial distribution of potassic alteration comprising a rock volume much larger than previously recognized during exploration. These results could imply either that the blind test was dealing with a giant porphyry deposit, with potassic alteration extending laterally over > 2 km, or that there was more than one smaller magmatic-hydrothermal center, producing two clusters of K-feldspar alteration separated by ~2 km.

Pyrite veins with muscovite halos overprinted the epidote-chlorite altered volcanoclastic rocks at the bottom of RT006 (Figs. 6G-L). Halloysite is a low-temperature clay mineral and is commonly considered a near-surface supergene alteration feature (e.g., Hedenquist et al., 1998), but it has been detected at considerable depths in some porphyry systems where it is inferred to have a hypogene origin (e.g., Kyne et al., 2013; Jansen et al., 2017). The presence of halloysite in the deepest samples from drill hole RT006 at Resolution (Table 3; Figs. 6G-L) therefore provides evidence of late-stage low-temperature acidic fluids, presumably of magmatic-hydrothermal origin. Muscovite implies higher-temperature moderately acidic conditions and typically occurs in an alteration plume above a porphyry deposit center (e.g.,

Halley et al., 2015), but can also be telescoped onto the potassic core of a deposit (Sillitoe, 2010).

Concerning the SWIR data, the pattern of decreasing 2,250 nm values with increasing depth at Resolution (Fig. 7D) is consistent with the findings of Neal et al. (2018) at Batu Hijau, Indonesia. They detected higher 2,250 nm feature wavelengths from chlorite-epidote-altered samples distal to Batu Hijau, with values as low as 2,243 nm characterizing the center of the deposit. The spatial variations of 2,250 nm values at Resolution imply a hydrothermal center at depth, if the SWIR responses are behaving in the same fashion as detected at Batu Hijau.

To summarize, from the perspective of a blind test assessment, collectively, the mineralogical, whole rock geochemical and SWIR data provide encouragement that the samples come from the propylitic halo to a porphyry deposit. The abundance of potassic alteration, sulfides and the presence of overprinting quartz-pyrite veins with muscovite alteration halos imply proximity to a porphyry deposit center, and if part of a single hydrothermal system, then the large spatial extent of K-feldspar alteration provides encouragement that the system may be a giant.

Epidote vectoring

The trace element chemistry of epidote varies with distance from porphyry deposits (Cooke et al., 2014). Epidote from locations proximal to a porphyry deposit center is comparatively depleted in As, Sb and Pb relative to epidote from more distal locations, and contains traces of detectable Cu, Mo, Sn, Bi, LREE and Zr (Cooke et al., 2014).

Figure 16 is a compilation of epidote trace element chemistry from several giant and small porphyry Cu deposits. The epidote data from Resolution are comparable to the range of trace element concentrations analyzed from epidotes collected within 0.7–1.5 km of a porphyry

deposit center, consistent with the conclusion that the blind test samples are all relatively proximal.

Epidote fertility assessment

Cooke et al. (2014) speculated that the largest porphyry deposits flux the most metals and argued that this is recorded in the trace element geochemistry of the distal propylitic alteration minerals, with greater distal pathfinder metal contents detected in epidote peripheral to larger deposits, providing a potential fertility assessment tool for explorers. This relationship is highlighted in Figure 17, which compares epidote LA-ICP-MS data from Resolution to datasets from several porphyry systems, including the giant El Teniente, Rosario, Ujina and Quebrada Blanca Cu-Mo deposits, Chile (Wilkinson et al., this volume; Baker et al, this volume), the giant Batu Hijau porphyry Cu-Au deposit, Indonesia, and small porphyry Cu-Au deposits at Black Mountain, Philippines (Cooke et al., 2014), and E48 and E26, Australia (Pacey et al., this volume a and b), along with data for metamorphic epidote from andesites of the central Chile porphyry province, amphibolite facies orthogneisses of the Harts Range and meta-andesites of the greenschist facies Georgetown Inlier, Australia (Baker et al., 2017). Overall, epidote from the giant porphyry deposits is characterized by As and Sb contents that are one or more orders of magnitude greater than epidote from small porphyry deposits. Baker et al. (2017) showed that metamorphic epidote is characterized by very low As and Sb (commonly below detection limits), low Mn and high Yb, and can be readily discriminated from porphyry epidote in most cases (Fig. 17; also see Wilkinson et al., this volume).

Overall, epidote from Resolution has lesser pathfinder element contents than epidote from the giant porphyry Cu-Mo deposits shown in Figure 17. Instead, the range of metal contents in epidote are comparable to the giant Batu Hijau porphyry Cu-Au deposit, and/or to the several small porphyry Cu-Au deposits shown. From a fertility assessment perspective, these

data could be interpreted to indicate that the blind test samples come from a small porphyry system. Fertility assessments using epidote chemistry may be compromised, however, by limited sample coverage. Ideally, sampling needs to extend to background, so that all geochemical domains around the porphyry system are analyzed, including the proximal sulfide-bearing and distal sulfide-deficient domains. The coexistence of pyrite and epidote and the widespread occurrence of K-feldspar alteration in many of the Resolution samples provided for the blind test suggests that they are mostly proximal samples. Because sampling did not extend far beyond the potassic and pyrite halos, it is therefore unlikely to have reached the geochemical background.

Cooke et al. (2014) noted that there are geochemical domains in the propylitic halo to porphyry deposits where competition for trace elements occurs between co-precipitating mineral phases. Chalcophile elements such as As and Sb are more likely to be incorporated into pyrite than epidote when these minerals co-precipitate, resulting in an inner pyrite-bearing domain of As- and Sb-depleted epidote, and a distal pyrite-absent domain of As- and Sb-enriched epidote. Figure 13 shows that where pyrite and epidote coexist in the blind test sample suite, pyrite is strongly enriched in chalcophile elements such as Co, As and Pb relative to epidote, and the coexisting epidote is enriched in Sn and Mn relative to pyrite.

Figure 18 compares the As and Sb contents of epidote from Resolution to data from several porphyry deposits, including giant Cu-Mo (El Teniente, Collahuasi district), giant Cu-Au (Batu Hijau), small Cu-Au (Black Mt, E48, E26) and metamorphic epidote. Distal epidote samples from the giant Cu-Mo systems locally have epidote with extreme As and Sb contents (> 1,000 ppm). High As and Sb in epidote are therefore considered strong indicators of a district's fertility with regards the potential for the presence of a giant porphyry deposit (Fig. 18). Distal epidote from small porphyry deposits typically has As and Sb contents in the range of 10–100 ppm, which is the same range as proximal epidotes from giant porphyry

deposits (Fig. 18). Metamorphic epidote plots in the bottom left corner of Figure 18, with many analyses not plotting because Sb is below detection limits. The Resolution blind test epidotes plot in the lower left part of the porphyry data cloud, and therefore could be interpreted either as epidote collected from close to a giant porphyry deposit, or distal to a small porphyry deposit (Fig. 18). The former interpretation was preferred in this case, given the coexistence of epidote and pyrite in many of the samples, the observations of widespread K-feldspar and chalcopyrite alteration, and increasing Cu contents towards the bottom of DDH RT006 (Fig. 7B).

Chlorite vectoring

Figure 15 illustrates that chlorite compositions at Resolution vary systematically with depth. Titanium substitutes into the chlorite crystal structure at high temperatures (Wilkinson et al., 2015), and the greatest titanium contents occur in the deepest drill hole samples in both the northern and southern clusters. Many of the distal pathfinder elements (e.g., Pb, Mn, Li) along with other trace elements such as Sr and Co, are enriched in chlorite samples from the highest elevations (Figs. 15 B-F) and are interpreted to have been incorporated into chlorite at lower temperatures and/or from less acidic and more reduced fluids. Chlorite proximator ratios, developed for Batu Hijau by Wilkinson et al. (2015), all increase systematically with depth at Resolution (Figs. 15 G-J).

Chlorite proximator calculations enable prediction of the distance to the center of the thermal anomaly associated with an intrusive complex (Wilkinson et al., 2015). Those distances can be in any direction, and so it is necessary to combine distance estimates from multiple samples to pinpoint the heat source. A simple approach to portraying the results of proximator calculations in two dimensions (assuming isotropic conditions) is to plot a circle surrounding the sample location, with the radius of the circle equating to the calculated distance to the deposit center (Fig. 19).

Applying the Ti/Sr chlorite proximator equation for Batu Hijau of Wilkinson et al. (2015) to the blind test sample suite gave a coherent result, precisely locating Resolution at depth between the two sample clusters, with a target defined in an area of approximately 400 m width, with spatial coordinates centered on 4,683,375 N and 494,300 E (Fig. 19). After revealing this result to Rio Tinto Exploration, they confirmed the success of the blind test in locating the ore deposit by generating Figure 20, which shows the location of the blind test target relative to the location of the ore zone on section 494,300 E.

The chlorite proximator of Wilkinson et al. (2015) is considered to detect the center of the thermal anomaly associated with a porphyry ore system, and this is an important factor to consider when assessing why the chlorite data pinpointed a location central to, but below, the Resolution ore zone (Fig. 20). The center of the thermal anomaly in a porphyry system should coincide with the porphyry intrusion or center of an intrusive complex and therefore would provide a valid target in X-Y coordinates. However, the thermal maximum to which the mineral chemistry is responding to is likely to be related to magmatic temperatures and therefore would be located beneath the ore zone because copper sulfides precipitate primarily in response to declining fluid temperatures, mainly between 450–300°C (e.g., Landtwing et al., 2005; 2010). Other factors that can influence the successful application of the chlorite proximator are that the size of the thermal anomaly can be influenced both by the size and geometry of the intrusive complex / thermal anomaly, and the orientation of the sample suite relative to the intrusive complex. In this case, it appears that a similar thermal gradient characterizes Resolution and Batu Hijau (consistent with their similar resource tonnages and ore zone dimensions; cf. Wilkinson et al., 2015), and so the Batu Hijau proximator is an appropriate calibration for the Resolution blind test suite. Importantly, the Resolution blind test was fortuitously optimized by Rio Tinto Exploration by providing a sample transect that

passed directly over the ore zone (Fig. 2). A more tangential traverse would have led to a subdued, more difficult to interpret, proximator result.

The combination epidote and chlorite mineral geochemistry was beneficial at Resolution because the chlorite data provided a strong indication of proximity, helping to resolve any ambiguity in the epidote fertility assessment by providing additional confidence in the interpretation that the subdued As-Sb response of epidote was due to proximity. Together, the two minerals gave indications of the fertility of the system from twelve samples and provided a robust drill target located between the two clusters of drill holes and at elevations several hundred meters below the deepest analyzed sample (Fig. 19). In a real-world situation, drilling of this mineral chemistry target would have led to the discovery of the Resolution orebody (Fig. 20). Rio Tinto Exploration have subsequently conducted a duplicate blind test of the Resolution result, using their own samples and in-house analytical laboratories, and confirmed the blind test result. Their testing has provided further confidence in LA-ICP-MS mineral chemistry as a tool for detecting the subtle, low-level hypogene geochemical anomalies preserved in propylitic minerals distal to porphyry centers, and provides further validation of their applicability to porphyry exploration.

Conclusions

The Resolution blind site test highlights the potential for mineral chemistry analyses to augment insights gained from routine geological and geochemical analyses in porphyry exploration in the green rock environment. As the Resolution blind test samples were taken mostly from within the pyrite halo of the porphyry deposit, the epidote data were not as effective at highlighting fertility of this system as in other cases, due to the competition for distal pathfinder elements between pyrite and epidote (Fig. 13). From a vectoring perspective, epidote compositions were consistent with the samples being located within 0.7–1.5 km of a porphyry center (Fig. 16). The chlorite proximator ratios of Wilkinson et al. (2015) gave

strong, coherent results, implying that the porphyry was located at depth (Fig. 19). Drilling of this target would have resulted in the discovery of Resolution (Fig. 20).

Mineral chemistry techniques show considerable promise for porphyry exploration and are now being applied to diverse environments that host porphyry and epithermal deposits around the circum-Pacific. Hypogene low-level trace element dispersion patterns preserved in propylitic alteration minerals such as epidote and chlorite have relevance to exploration under post-mineralization cover, as well as in areas where outcrop is limited and only the distal fringes of the alteration systems are exposed, although challenges in data interpretation may arise if a prospect has been tilted (e.g., Yerington, Ajo, Hall) or substantially eroded (El Abra, Radomiro Tomić, Sierrita, Bagdad). Epidote and chlorite LA-ICP-MS analyses have the potential to provide a method of reconnaissance geochemical screening with a broadly-spaced sample distribution, which ideally should be conducted early in the assessment of porphyry districts, in conjunction with routine geological, geophysical and geochemical exploration methods. Mineral chemistry analyses can provide explorers with methods to help target blind deposits at depth from only limited numbers of surface or shallowly drilled samples.

Acknowledgements

Our research into the geochemical footprints of porphyry and epithermal deposits has been supported through five AMIRA International projects since 2004: P765, P765A, P1060, P1153 and P1202, and we thank our sponsors for their sustained support. The results presented here are derived from AMIRA International project P765A and we thank all sponsors and other team members of that project, in particular Alan Goode, Adele Seymon, Jeff Hedenquist, Nic Jansen, Gabe Sweet and Roisin Kyne. We also thank Karsten Goemann, Sandrin Feig and colleagues at the Central Science Laboratory, University of Tasmania for their assistance in mineral chemistry analyses and imaging. Adam Schwartz and Anthony

Henager from Resolution Copper are thanked for sample collection and shipping. Dave Braxton is thanked for advice on global copper consumption and production.

References

- Ahmed, A.D., Fisher, L., Pearce, M., Escolme, A., Cooke, D.R., Howard, D., and Belousov, I., this volume, A microscale analysis of hydrothermal epidote using XFM and XANES: Implications for the use of LA-ICP-MS mineral chemistry in complex alteration environments: *Economic Geology*, this volume.
- Alva-Jimenez, T., Tosdal, R.M., Dipple, G., Dilles, J.H., Kent, A.J.R., and Halley, S., this volume, Chemical variations in hydrothermal muscovite across the Highland Valley porphyry Cu-Mo district, British Columbia, Canada: *Economic Geology*, this volume.
- Baker, M., Cooke, D.R., Hollings, P., and Piquer, J., 2017, Identification of hydrothermal alteration related to mineralisation using epidote mineral chemistry: *Society of Geology Applied to Ore Deposits*, 14th Biennial Conference Proceedings, Quebec, v. 3, 1069–1071.
- Baker, M.J., Wilkinson, J.J., Wilkinson, C.C., Cooke, D.R. and Ireland, T.J., this volume, Epidote trace element chemistry as an exploration tool: a case study from the Collahuasi district, northern Chile: *Economic Geology*, this volume.
- Ballard, J.R., Palin, J.M., and Campbell, I.H., 2002, Relative oxidation states of magmas inferred from Ce(IV)/Ce(III) in zircon: Application to porphyry copper deposits of northern Chile: *Contributions to Mineralogy and Petrology*, v. 144, p. 347–364.
- Bright, R.M., Amato, J.M., Denyszyn, S.W., and Ernst, R.E., 2014. U-Pb geochronology of 1.1 Ga diabase in the southwestern United States: Testing models for the origin of a post-Grenville large igneous province: *Lithosphere*, v. 6, p. 135–156.
- Byrne, K., Lesage, G., Gleeson, S.A., Piercey, S.J., Lypaczewski, P., and Kyser, K., this volume-A, Linking mineralogy to lithochemical changes and C isotope composition in

- rocks around the Highland Valley Copper porphyry district – Implications for porphyry Cu footprints: *Economic Geology*, this volume.
- Byrne, K., Lesage, G., Gleeson, S.A., Trumbull, R.B., Ryan, J., Kyser, K., and Lee, R.G., this volume-B, Mineralogical and isotopic characteristics of sodic-calcic alteration in the Highland Valley Copper district, British Columbia, Canada – Implications for fluid sources in porphyry Cu systems: *Economic Geology*, this volume.
- Cao, M.J., Hollings, P., Evans, N.J., Cooke, D.R. McInnes, B.I.A., Zhao, K.D., Qin, K.Z., and Li, D.F., this volume, In situ elemental and Sr isotopic characteristics of magmatic to hydrothermal minerals from the Black Mt porphyry deposit, Baguio District, Philippines: implications for the magmatic to hydrothermal formation processes: *Economic Geology*, this volume.
- Chaffee, M.A., 1982a, A geochemical study of the Kalamazoo porphyry deposit, Pinal County, Arizona, in Titley, S.R., ed., *Advances in geology of the porphyry copper deposits, southwestern North America*: Tucson, University of Arizona Press, p. 211–225.
- Chaffee, M.A., 1982b, Geochemical prospecting techniques for porphyry copper deposits, southwestern United States and Northern Mexico, in Titley, S.R., ed., *Advances in geology of the porphyry copper deposits, southwestern North America*: Tucson, University of Arizona Press, p. 297–307.
- Chang, Z., Hedenquist, J.W., White, N.C., Cooke, D.R., Roach, M., Deyell, C.L., Garcia, J., Gemmell, J.B., McKnight, S., and Cuisson, A.L., 2011, Exploration tools for linked porphyry and epithermal deposits: Example from the Mankayan intrusion-centered Cu-Au district, Luzon, Philippines: *Economic Geology*, v. 106, p. 1365–1398.
- Condie, K.C., and De Melas, J.P., 1985, The Pinal Schist: An early Proterozoic quartz wacke association in southeastern Arizona: *Precambrian Research*, v. 27, p. 337–356.

- Cooke, D.R., Baker, M., Hollings P., Sweet, G., Chang, Z., Danyushevsky, L., Gilbert, S., Zhou, T., White, N.C., Gemmell, J.B., and Inglis, S., 2014, New advances in detecting the distal geochemical footprints of porphyry systems – epidote mineral chemistry as a tool for vectoring and fertility assessments: Society of Economic Geologists, Special Publication 18, p. 127–152
- Cooke, D.R., Agnew, P., Hollings, P., Baker, M., Chang, Z., Wilkinson, J.J., Ahmed, A., White, N.C., Zhang, L., Thompson, J., Gemmell, J.B., and Chen, H., 2020, Recent advances in the application of mineral chemistry to exploration for porphyry copper–gold–molybdenum deposits: detecting the geochemical fingerprints and footprints of hypogene mineralization and alteration: *Geochemistry: Exploration, Environment, Analysis*, in press.
- Cross, A.J., 2000, An investigation of the minor and trace element chemistry of hydrothermal porphyry and skarn-related magnetite: Ph.D. thesis, Canberra, Australia, University of Canberra, 171 p.
- Dilles, J.H., Kent, A.J.R., Wooden, J.L., Tosdal, R.M., Koleszar, A., Lee, R.G., and Farmer, L.P., 2015, Zircon compositional evidence for sulfur-degassing from ore-forming arc magmas: *Economic Geology*, 110, 241–251.
- Dupuis, C., and Beaudoin, G., 2011, Discriminant diagrams for iron oxide trace element fingerprinting of mineral deposit types: *Mineralium Deposita*, 46, 319–335.
- Eisele, J., and Isachsen, C.E., 2001, Crustal growth in southern Arizona: U-Pb geochronologic and Sm-Nd isotopic evidence for addition of Paleoproterozoic Cochise block to the Mazatzal Province: *American Journal of Science*, v. 301, p. 773–797.
- Emmons, W.H., 1927, Relations of the disseminated copper ores in porphyry to igneous intrusives: *American Institute of Mining Metallurgists and Engineers Transactions*, 75, p. 797–815.

- Friehauf, K.C., 1998, Geology and geochemistry of porphyry-related, carbonate-hosted massive replacement Cu-Au deposits – A case study of the Superior district, Arizona: Unpublished Ph.D. thesis, Stanford, USA, Stanford University, 221 p.
- Friehauf, K.C., and Pareja, G.A., 1998, Can oxygen isotope halos be produced around high-temperature dolostone-hosted ore deposits?; evidence from the Superior District, Arizona: *Economic Geology*, v. 93, p. 639–650.
- Gustafson, L. B., 1961, Paragenesis and hypogene zoning at the Magma mine, Superior, Arizona: Unpublished Ph.D. thesis, Cambridge, USA, Harvard University, 93 p.
- Gustafson, L.B., and Hunt, J.P., 1975, The porphyry copper deposit at El Salvador, Chile: *ECONOMIC GEOLOGY*, v. 70, p. 857–912.
- Halley, S., Dilles, J.H., and Tosdal, R.M., 2015, Footprints: hydrothermal alteration and geochemical dispersion around porphyry copper deposits: *SEG Newsletter*, No. 100, p. 1, 12–17.
- Heaman, L.M., Easton, M., Hart, T.R., Hollings, P., MacDonald, C.A., and Smyk, M., 2007. Further refinement to the timing of Mesoproterozoic magmatism, Lake Nipigon Region, Ontario. *Canadian Journal of Earth Sciences*, v. 44, p. 1055–1086.
- Hedenquist, J.W., Arribas, A., Jr., and Reynolds, T.J., 1998, Evolution of an intrusion-centred hydrothermal system: Far southeast-Lepanto porphyry and epithermal Cu-Au deposit, Philippines: *Economic Geology*, v. 93, p. 373–404.
- Hehnke, C., Ballantyne, G., Martin, H., Hart, W., Schwarz, A., and Stein, H., 2012, Geology and exploration progress at the Resolution porphyry Cu-Mo deposit, Arizona: *Society of Economic Geologists Special Publication 16*, p. 147–166.
- Holliday, J.R., and Cooke, D.R., 2007, Advances in geological models and exploration methods for copper ± gold porphyry deposits: *Fifth Decennial International Conference on Mineral Exploration 5*, Toronto, p. 791–809.

- Jansen, N.H., Gemmell, J.B., Chang, Z., Cooke, D.R., Jourdan, F., Creaser, R.A., and Hollings, P., 2017, Geology and genesis of the Cerro la Mina porphyry-high sulfidation Au (Cu-Mo) prospect, Mexico: *Economic Geology*, v. 112, p. 799–827.
- Kyne, R., Hollings, P., Jansen, N.H., and Cooke, D., 2013, Supergene and hypogene halloysite in a porphyry-epithermal environment at Cerro la Mina, Chiapas, Mexico: *Economic Geology*, v. 108, p. 1147–1161.
- Landtwing, M.R., Furrer, C., Redmond P.B., Pettke, T., Guillong, M., Heinrich, C.A., 2010, The Bingham Canyon porphyry Cu–Mo–Au deposit; III, Zoned copper-gold ore deposition by magmatic vapor expansion: *Economic Geology*, v. 105, p. 91–118.
- Landtwing, M.R., Pettke, T., Halter, W.E., Heinrich, C.A., Redmond, P.B., Einaudi, M.T., and Kunze, K., 2005, Copper deposition during quartz dissolution by cooling magmatic-hydrothermal fluids: The Bingham porphyry: *Earth and Planetary Science Letters*, v. 235, p. 229–243.
- Large, R.R., Gemmell, J.B., Paulick, H., and Huston, D.L., 2001, The alteration box plot: A simple approach to understanding the relationship between alteration mineralogy and lithogeochemistry associated with volcanic-hosted massive sulfide deposits: *Economic Geology*, v. 96, p. 957–971.
- Large, R.R., Danyushevsky, L.D., Hollit, C., Maslennikov, V.V., Meffre, S., Gilbert, S., Bull, S., Scott, R., Emsbo, P., Thomas, H., Singh, R., Foster, J., 2009, Gold and trace element zonation in pyrite using a laser imaging technique; Implications for the timing of gold in orogenic and Carlin-style sediment-hosted deposits: *ECONOMIC GEOLOGY* v. 104, p. 635–668.
- Loader, M.A., Wilkinson, J.J., and Armstrong, R.N., 2017, The effect of titanite crystallisation on Eu and Ce anomalies in zircon and its implications for the assessment of porphyry Cu deposit fertility: *Earth and Planetary Science Letters*, v. 472, p. 107–119.

- Manske, S.L., and Paul, A.H., 2002, Geology of a major new porphyry copper center in the Superior (Pioneer) district, Arizona: *Economic Geology*, v. 97, p. 197–220.
- Mao, M., Rukhlov, A.S., Rowins, S.M., Spence, J., and Coogan, L.A., 2016, Apatite trace element compositions: A robust new tool for mineral exploration: *Economic Geology*, 111, p. 1187–1222.
- McCarrel, M.J., 2012, Characterization and correlation of skarn mineralization and protoliths, Resolution porphyry copper deposit, Superior district, Arizona: Unpublished MSc thesis, Tucson, USA, University of Arizona, 51 p.
- McConnell, R.L., 1975, Biostratigraphy and depositional environment of algal stromatolites from the Mescal Limestone (Proterozoic) of central Arizona: *Precambrian Research*, v. 2, p. 317–328.
- Miller, J.D., Nicholson, S.W., Easton, R.M., Ripley, E.M., and Feinberg, J., 2013, The geology and mineral deposits of the 1.1 Ga Midcontinent Rift in the Lake Superior region – An overview; *in* Miller, J.D., ed., *Field guide to the Cu-Ni-PGE deposits of the Lake Superior Region*; *Precambrian Research Center Guidebook 13-1*, p. 1–50.
- Mulder, J.A., Karlstrom, K.E., Fletcher, K., Heizler, M.T., Timmons, J.M., Crossey, L.J., and Pecha, M., 2017, The syn-orogenic sedimentary record of the Grenville Orogeny in southwest Laurentia: *Precambrian Research*, v. 294, p. 33–52.
- Nadoll, P., Mauk, J.L., Leveille, R.A., and Koenig, A.E., 2015, Geochemistry of magnetite from porphyry Cu and skarn deposits in the southwestern United States: *Mineralium Deposita*, 50, p. 493–515.
- Neal, L.C., Wilkinson, J.J., Mason, P.J., and Chang, Z., 2018 Spectral characteristics of propylitic alteration minerals as a vectoring tool for porphyry copper deposits: *Journal of Geochemical Exploration*, v. 184, p. 179–198.

- Pacey, A., Wilkinson, J.J., and Cooke, D.R., this volume a; Chlorite and epidote mineral chemistry in porphyry ore systems: A case study of the Northparkes district, NSW, Australia: *Economic Geology*, this volume.
- Pacey, A., Wilkinson, J.J., Boyce, A., and Millar, this volume b; Oxygen, hydrogen and strontium isotopic constraints on the origin of propylitic alteration in porphyry deposits: Insights from the Northparkes district, NSW, Australia: *Economic Geology*, this volume.
- Paul, A.H., and Knight, M.J., 1995, Replacement ores in the Magma mine, Superior, Arizona, *in* Pierce, F.W., and Bolm, J.G., eds., *Porphyry copper deposits of the American Cordillera: Arizona Geological Society Digest 20*, p. 366-372.
- Pearce, J.A., 1996, A user's guide to basalt discrimination diagrams. Trace element geochemistry of volcanic rocks; applications for massive sulphide exploration: Geological Association of Canada, *Short Course Notes*, v. 12, p. 79–113.
- Peccerillo, A., and Taylor, S.R., 1976, Geochemistry of Eocene calc-alkaline volcanic rocks from the Kastamonu area, northern Turkey: *Contributions to Mineralogy and Petrology*, v. 58, p. 63–81.
- Peterson, D. W., 1969, Geologic map of the Superior quadrangle, Pinal County, Arizona: U.S. Geological Survey Geologic Quadrangle Map GQ-818, scale 1: 24,000.
- Pietrzyk S., and Tora 2018, B., Trends in global copper mining – a review: *IOP Conference Series, Materials Science and Engineering* 427, 012002 doi:10.1088/1757–899X/427/1/012002.
- Phillips, J., 2019, Geologic and geochemical vectors to mineralisation at the Resolution porphyry Cu-Mo deposit, Arizona: Unpublished Ph.D. thesis, Hobart, Australia, University of Tasmania, 370 p.
- Pontual, S., 2010, Spectral reflectance datasets: Processing, interpretation and analysis for mining and exploration applications: AusSpec International Ltd, *Spectral Geology*

- Workshop Notes, Institut national de la recherche scientifique, Québec City, Canada, 2010, 49 p.
- Post, J.L., and Noble, P.N., 1993, The near-infrared combination band frequencies of dioctahedral smectites, micas, and illites: *Clays and Clay Minerals*, v. 41, p. 639–644.
- Rickwood, P.C., 1989, Boundary lines within petrologic diagrams which use oxides of major and minor elements: *Lithos*, v. 22, p. 247–263.
- Rinne, M.L., Cooke, D.R., Harris, A.C., Finn, D.J., Allen, C.M., Heizler, M.T., and Creaser, R.A., 2018, Geology and geochronology of the Golpu porphyry and Wafi epithermal deposit, Morobe Province, Papua New Guinea: *Economic Geology*, v. 113, p. 271–294.
- Rio Tinto Annual Report, 2018:
http://www.riotinto.com/documents/RT_2018_annual_report.pdf
- Schwarz, A., 2007, Geology of the Resolution porphyry Cu-Mo system: Ores and orogenesis: A symposium honoring the career of William R. Dickinson: Arizona Geological Society, Tucson, September 2007, Program with Abstracts, p. 83–84.
- Schwarz, A., 2010, Early diabase-hosted alteration-mineralization in the Resolution Cu-Mo deposit, Pinal County, Arizona: The foundation of a giant porphyry system: Unpublished Ph.D. thesis, Tucson, USA, University of Arizona, 153 p.
- Schott, T.G., 1994, Mineralization, lithology, and alteration in the Mesozoic rocks, Superior mine, Superior, Arizona: Unpublished M.Sc. thesis, Socorro, USA, New Mexico Institute of Mining and Technology, 197 p.
- Scott, K.M., and Yang, K., 1997, Spectral reflectance studies of white micas: Commonwealth Scientific and Industrial Research Organisation, Exploration and Mining Report 439R, 35 p.
- Sell, J.D., 1995, Discovery of a deep (3500 feet) unexposed porphyry copper deposit at Superior East, Pinal County, Arizona, *in* Pierce, F.W., and Bolm, J.G., eds., *Porphyry*

- copper deposits of the American Cordillera: Arizona Geological Society Digest, v. 20, p. 373–395.
- Short, M. N., Galbraith, F. W., Harshman, E. N., Kuhn, T. H., and Wilson, E. D., 1943, Geology and ore deposits of the Superior mining area, Arizona: Arizona Bureau of Mines and Geology Series no. 16, Bulletin 151, 159 p.
- Shride, A.F., 1967, Younger Precambrian geology in southern Arizona: U.S. Geological Survey Professional Paper 566, 89 p.
- Sillitoe, R.H., 2010, Porphyry copper systems: ECONOMIC GEOLOGY, v. 105, p. 3-41.
- Spencer, J.E. and Reynolds, S.J., 1989, Middle Tertiary tectonics of Arizona and adjacent areas, *in* Jenny J.P., and Reynolds, S.J eds., Geologic Evolution of Arizona: Arizona Geological Survey Digest 17, p. 539–573.
- Stanley, C.R., and Madeisky, H.E., 1996, Lithogeochemical exploration for metasomatic zones associated with hydrothermal mineral deposits using molar element ratio analysis: Introduction, Lithogeochemical Exploration Research Project, Mineral Deposit Research Unit, University of British Columbia, Short Course Notes, 200 p.
- Troutman, S.M., 2001, Advanced argillic alteration in the deeply buried Magma porphyry Cu-Mo prospect, Superior, Arizona: Unpublished MSc. thesis, Stanford, USA, Stanford University, 115 p.
- United States Geological Survey, 2019, Copper statistics and information: National Minerals Information Center, <https://www.usgs.gov/centers/nmic/copper-statistics-and-information>.
- Uribe-Mogollon, C., and Maher, K., 2018, White mica geochemistry of the Copper Cliff porphyry Cu deposit: Insights from a vectoring tool applied to exploration: Economic Geology v. 113, p. 1269–1295.

- Wilkinson, J.J., Chang, Z., Cooke, D.R., Baker, M.J., Wilkinson, C.C., Inglis, S., Chen, H., and Gemmell, J.B., 2015, The chlorite proximator: A new tool for detecting porphyry ore deposits: *Journal of Geochemical Exploration*, v. 152, p. 10–26.
- Wilkinson, J.J., Baker, M.J., Cooke, D.R. and Wilkinson, C.C., this volume, Exploration targeting in porphyry Cu systems using propylitic mineral chemistry: a case study of the El Teniente deposit, Chile: *Economic Geology*, this volume.
- Williamson, B.J., Herrington, R.J., and Morris, A., 2016, Porphyry copper enrichment linked to excess aluminium in plagioclase: *Nature Geosciences*, 9, p. 237–242.
- Winant, A.R., 2010, Sericitic and advanced argillic mineral assemblages and their relationship to copper mineralization, Resolution porphyry Cu-(Mo) deposit, Superior District, Pinal County, Arizona: Unpublished MSc. thesis, Tucson, USA, University of Arizona, 54 p.
- Wrukke, C.T., 1989, The Middle Proterozoic Apache Group, Troy Quartzite, and associated diabase of Arizona, *in* Jenney, J.P., and Reynolds, S.J., eds., *Geologic Evolution of Arizona: Arizona Geological Society Digest*, v. 17, p. 239–258.
- Yang, K., Huntington, J.F., Gemmell, J.B., and Scott, K.M., 2011, Variations in composition and abundance of white mica in the hydrothermal alteration system at Hellyer, Tasmania, as revealed by infrared reflectance spectroscopy: *Journal of Geochemical Exploration*, v. 108, p. 143–156.

Figure Captions

Figure 1: Spatial distribution of the twelve blind test samples from Resolution. A) Plan view. B) Sample locations on section 494,300 E (looking west). Section location shown in A. Samples have been projected up to 300 m onto the section. The samples can be divided into northern and southern clusters, separated spatially by approximately 2 km. The northern samples were all collected from one drill hole (DDH RT006). Rock types are taken from the sample ledger provided by Rio Tinto Exploration. Sample coordinates are provided in Table 1.

Figure 2: Geology of the Superior District, compiled from Peterson (1969), Spencer and Reynolds (1989), Hehnke et al. (2012) and Phillips (2019), including the locations of past producing mines and major undeveloped orebodies. Red dots represent sample locations.

Abbreviations: AF = Anxiety fault; CF = Concentrator fault; CSF = Conley Springs fault; DCF = Devils Canyon fault; LS and A = Lake Superior and Arizona mine; MF = Main fault; NBF = North Boundary fault; SBF = South Boundary fault; WBF = West Boundary fault.

Figure 3: Schematic stratigraphic column of the Superior District. Modified after Hammer (pers. commun., 1973) and Phillips (2019).

Figure 4: Samples of propylitic- and potassic-altered rocks from the southern cluster of Resolution blind test samples, including the shallowest northern sample. Images A, C, E, G, I and K show polished ~1-cm thick slab faces, whereas images B, D, F, H, J and L are the corresponding unpolished and sodium cobaltinitrite-stained back sides of each sample, respectively. The stained samples are shown as mirror images to allow ease of comparison between each image pair. (A–B) Sample 10046363: medium- to coarse-grained Proterozoic dolerite with patchy epidote–calcite alteration of magmatic plagioclase, and chlorite–pyrite alteration of magmatic pyroxene. Staining has highlighted the selective moderate K-feldspar alteration of plagioclase in image B that was not apparent in image A. (C–D) Sample

10046364: Medium- to coarse-grained Proterozoic dolerite with patchy epidote–calcite after plagioclase, and chlorite after pyroxene. Staining revealed selective moderate K-feldspar alteration of plagioclase. This sample lacks pyrite. (E–F) Sample 10046360: Matrix-rich polymict lithic breccia with angular to rounded clasts of quartz-hornblende-plagioclase-phyric dacite, and minor andesite and mudstone clasts. Selective epidote alteration has affected the clasts and plagioclase crystal fragments, whereas chlorite–pyrite alteration has affected the matrix. Staining highlights intense K-feldspar alteration of the matrix, smaller clasts, and plagioclase crystals, but only the outer rind of the oversized (9 cm diameter) dacite clast on the left side of the images was altered to K-feldspar. (G–H) Sample 10046361: Crystal-lithic-rich volcanoclastic breccia with selective epidote alteration of plagioclase crystals, chlorite–pyrite alteration of hornblende, and intense, selective K-feldspar alteration of the matrix and smaller clasts. (I–J) Sample 10046362: Matrix-rich polymict lithic breccia with patchy epidote–chlorite–pyrite–hematite–calcite alteration and abundant 2–3 mm disseminated pyrite cubes. Intense, pervasive K-feldspar alteration has affected the matrix and many clasts. (K–L) Sample 10046353: Pebbly crystal-lithic sandstone with weak, selective epidote–chlorite–hematite–calcite alteration of andesitic lithic clasts and plagioclase crystals. Staining revealed only rare K-feldspar crystals (magmatic?). This sample lacks pyrite. Abbreviations: cal = calcite; chl = chlorite; ep = epidote; Kf = K-feldspar; py = pyrite.

Figure 5: Simplified NW-SE cross section (view NE) through the Resolution half-graben showing relationships between major fault blocks and location of the 1% copper ore shell on this section. The section location is shown on Figure 2. Also shown are the projected locations of the blind test samples (red filled circles) and drill hole traces that the samples were taken from. Please note that the samples have been projected up to 300 m from off-section. The unconformity surface separating pre- and post-mineralization rocks dips shallowly eastwards, and the southern samples were projected onto this section

approximately 500 to 700 m from the west (Fig. 2). Abbreviations: NBF = North Boundary Fault; SBF = South Boundary Fault. Modified after Hehnke et al. (2012).

Figure 6: Samples of propylitic-, potassic- and phyllic-altered rocks from the northern drill hole (RT006). Images A, C, E, G, I and K show polished slabs, whereas images B, D, F, H, J and L are the corresponding unpolished and sodium cobaltinitrite-stained back sides of each sample, respectively. The stained samples are shown as mirror images to allow ease of comparison between each image pair. (A–B) Sample 10046354: Matrix-rich polymict lithic breccia with epidote–chlorite–hematite–calcite alteration of the matrix, some small clasts and the outer rind of the outsized (7 cm diameter) clast. Staining revealed intense, pervasive K-feldspar alteration of the large clast, and selective K-feldspar alteration of the matrix and some small clasts and crystal fragments. (C–D) Sample 10046355: Plagioclase-hornblende crystal-lithic tuff cut by chalcopyrite veinlets with biotite–K-feldspar alteration halos. Selective epidote–chlorite–pyrite alteration of clasts and some plagioclase and hornblende crystals. (E–F) Sample 10046356: Polymict lithic breccia cut by discontinuous epidote veinlet with K-feldspar alteration halo. Some clasts have been pervasively and intensely altered to epidote, and some have intense to moderate K-feldspar alteration. The matrix has undergone moderate chlorite–pyrite alteration. (G–H) Sample 10046357: Intense K-feldspar and patchy epidote–chlorite–pyrite alteration of polymict lithic crystal-rich breccia. A quartz-chalcopyrite-pyrite veinlet with a muscovite-pyrite alteration halo dusted by late halloysite has an outer K-feldspar halo, suggesting that an early potassic vein was reopened during phyllic alteration and then overprinted by late argillic alteration. (I–J) Sample 10046358: Crystal-rich volcanoclastic breccia cut by quartz–pyrite ± chalcopyrite veins with intense muscovite–halloysite alteration halos. The larger vein has an intense outer K-feldspar halo, suggesting reopening of a potassic stage vein. Away from the larger vein, the sample has undergone intense to moderate K-feldspar–biotite alteration and

patchy epidote–chlorite–pyrite alteration. (K–L) Sample 10046359: Polymict lithic breccia cut by numerous quartz–pyrite veinlets with muscovite–pyrite alteration halos dusted by late-stage halloysite. Some of the larger quartz–pyrite veins have outer halos of K-feldspar–chalcopyrite. Larger clasts have rinds of K-feldspar alteration, and some clasts have undergone patchy epidote–chlorite–pyrite alteration. Abbreviations: bi = biotite; cal = calcite; chl = chlorite; ep = epidote; Kf = K-feldspar; ms = muscovite; py = pyrite.

Figure 7. Spatial distribution of pyrite, chalcopyrite, and selected SWIR results on section 494,300 E (looking west). Section trace shown on Figure 1. (A) Pyrite occurrences in altered rocks and veins. Also shown are total sulfur contents (wt %) for each sample (data listed in Table 1). Total sulfur increases markedly towards the bottom of RT006, coincident with an increase in abundance of pyrite veins. (B) Spatial distribution of chalcopyrite, observed in veins and/or alteration halos, together with copper concentrations (ppm) for each sample (data listed in Table 2). Copper concentrations increase markedly towards the bottom of RT006, coincident with an increase in abundance of chalcopyrite-bearing veins. (C) SWIR results: 2,200 nm feature positions for muscovite and/or phengite-bearing spot analyses (data listed in Table 3). (D) SWIR results: 2,250 nm feature positions, highlighting variations in chlorite compositions (data listed in Table 3). Bins defined based on natural breaks.

Figure 8. Whole rock geochemistry of blind test samples from the Superior District. (A) K_2O vs. SiO_2 plot with fields for low-, medium- and high-K calc-alkaline rocks and shoshonites modified from Peccerillo and Taylor (1976) and Rickwood (1989). (B) Immobile trace element volcanic rock classification (Pearce, 1996). (C) Alteration box plot (Large et al. 2001). (D) Feldspar Na-K GER diagram (K/Al vs Na/Al molar ratio plot) adapted from Stanley and Madeisky (1996). Symbols on panels C and D are scaled based on loss on ignition (LOI) concentrations as a proxy for hydrous alteration, with large symbols indicating

high LOI values (maximum of 8.8 wt % LOI) and small symbols indicative of low values (minimum of 2.2 wt %). All data listed in Tables 1 and 2.

Figure 9. Spatial variations in whole rock geochemical data on section 494,300 E (looking west). (A) K₂O (wt %). (B) CaO (wt %). (C) TiO₂ (wt %). (D) Ni (ppm). All data listed in Tables 1 and 2. Bins defined based on natural breaks. Section trace shown on Figure 1.

Figure 10. Spatial variations in whole rock geochemical data (selected pathfinder elements) on section 494,300 E (looking west). (A) Cu (ppm). (B) Te (ppm). (C) Li (ppm). (D) Mn (ppm). (E) Zn (ppm). (F) Sb (ppm). All data listed in Table 2. Bins defined based on natural breaks.

Figure 11. LA-ICP-MS maps showing trace element deportments in a pyrite cube from an epidote–chlorite–pyrite- and K-feldspar-altered Cretaceous matrix-rich polymict lithic breccia (Sample 10046362; Fig. 4I; Table 3). The pyrite cube is hosted in a chlorite- and K-feldspar altered matrix. (A) ²⁴Mg. (B) ²⁷Al. (C) ²⁹Si. (D) ³⁹K. (E) ⁴⁹Ti. (F) ⁵¹V. (G) ⁵⁵Mn. (H) ⁵⁷Fe. (I) ⁵⁹Co. (J) ⁶⁰Ni. (K) ⁶⁵Cu. (L) ⁶⁶Zn. (M) ⁷⁵As. (N) ⁷⁷Se. (O) ⁹⁵Mo. (P) ¹⁰⁷Ag. (Q) ¹²⁵Te. (R) ¹⁸²W. (S) ¹⁹⁵Pt. (T) ¹⁹⁷Au. (U) ²⁰⁸Pb. (V) ²⁰⁹Bi. (W) ²³²Th. (X) ²³⁸U. Scale bars show counts per second results for each element analyzed, with high counts corresponding to high concentrations.

Figure 12. LA-ICP-MS maps showing trace element deportments in two pyrite grains from a Cretaceous crystal-rich volcanoclastic breccia that has undergone intense to moderate K-feldspar–biotite alteration and patchy epidote–chlorite–pyrite alteration. (Sample 10046358; Fig. 6I; Table 3). The pyrite grains are hosted in a chlorite- and K-feldspar altered matrix. (A) ²⁴Mg. (B) ²⁷Al. (C) ²⁹Si. (D) ³⁹K. (E) ⁴⁹Ti. (F) ⁵¹V. (G) ⁵⁵Mn. (H) ⁵⁷Fe. (I) ⁵⁹Co. (J) ⁶⁰Ni. (K) ⁶⁵Cu. (L) ⁶⁶Zn. (M) ⁷⁵As. (N) ⁷⁷Se. (O) ⁹⁵Mo. (P) ¹⁰⁷Ag. (Q) ¹²¹Sb. (R) ¹²⁵Te. (S) ¹⁸²W. (T) ¹⁹⁵Pt. (U) ¹⁹⁷Au. (V) ²⁰²Hg. (W) ²⁰⁸Pb. (X) ²⁰⁹Bi. (Y) ²³²Th. Scale bars show counts per second results for each element analyzed, with high counts corresponding to high concentrations.

Figure 13. Tukey box plot comparisons of pyrite and epidote LA-ICP-MS data (ppm), showing median (dot), mean (horizontal line within the box), 25th percentile and 75th percentile results, and far outliers. Results have been grouped and color-coded based on three spatial domains: (1) southern sample cluster (blue): 48 epidote and 23 pyrite analyses; (2) deep northern cluster (red): 88 epidote and 35 pyrite analyses; (3) shallow northern cluster (green): 32 epidote analyses. There is no pyrite in the shallow northern cluster of samples. Pyrite data are presented in A-C and G-I. The epidote data are presented in panels D-F and J-L, immediately below the corresponding pyrite graphs for comparative purposes. (A) Co in pyrite. (B) Sn in pyrite. (C) Mn in pyrite. (D) Co in epidote. (E) Sn in epidote. (F) Mn in epidote. (G) As in pyrite. (H) Pb in pyrite. (I) Sb in pyrite. (J) As in epidote. (K) Pb in epidote. (L) Sb in epidote. Pyrite data summarized in Table 4 and listed in Digital Appendix A2. Epidote data summarized in Table 5 and listed in Digital Appendix A3. Blue = southern samples. Red = deep northern samples. Green = shallow northern samples. Circles = outliers; triangles = far outliers. Abbreviations: ep = epidote; py = pyrite.

Figure 14: Spatial variations in average epidote trace element compositions on section 494,300 E (looking west). (A) As (ppm). (B) Sb (ppm). (C) Pb (ppm). (D) Mn (ppm). (E) Sn (ppm). (F) La (ppm). Epidote LA-ICP-MS data summarized in Table 5 and listed in Digital Appendix A3. Bins defined based on natural breaks.

Figure 15. Spatial variations in chlorite trace element compositions and proximator ratios on section 494,300 E (looking west). (A) Ti (ppm). (B) Li (ppm). (C) Sr (ppm). (D) Pb (ppm). (E) Co (ppm). (F) Mn (ppm). (G) Ti/Sr. (H) Ti/Li. (I) Ti/Co. (J) Ti/Mn. Chlorite LA-ICP-MS data summarized in Table 6 and listed in Digital Appendix A4. Bins defined based on natural breaks.

Figure 16: Tukey box plots showing a compilation of epidote LA-ICP-MS data from selected porphyry deposits plotted as a function of distance from the ore deposit center, with data divided into color bins based on 10 equal ranges (average of 220 analyses per bin). (A) As in

epidote. (B) Sb in epidote. (C) Pb in epidote. (D) U in epidote. At distances greater than 1 km from the deposit centers, there are systematic increases with distance for As, Sb and Pb contents of epidote, whereas U increases slightly over the first few hundred meters out from the center and then plateaus. Also shown are epidote data from the Resolution blind site (black fill, right hand side of each graph). The Resolution data are mostly comparable to epidote collected from between 0.7 and 1.5 km from the deposit center. Data sources: El Teniente from Wilkinson et al. (this volume; 610 analyses), Quebrada Blanca, Ujina, and Rosario from Baker et al. (this volume; 291, 189 and 154 analyses, respectively), Batu Hijau from Wilkinson et al. (2015; 255 analyses); Black Mountain from Cooke et al. (2014; 272 analyses); Endeavour 48 and Endeavour 26 from Pacey et al. (this volume a; 286 and 248 analyses, respectively), metamorphic epidote from Baker et al. (2017; 75 analyses); Resolution (Table 5; Digital Appendix A3; 374 analyses). Abbreviation: epi = epidote.

Figure 17: Tukey box plots comparing epidote LA-ICP-MS data from giant porphyry Cu-Mo deposits (El Teniente — Wilkinson et al., this volume; Quebrada Blanca, Ujina, and Rosario — Baker et al., this volume), giant porphyry Cu-Au (Batu Hijau; Wilkinson et al., 2015); small porphyry Cu-Au (Black Mountain from Cooke et al., 2014; Endeavour 48 and Endeavour 26 from Pacey et al., this volume a), metamorphic epidote (Baker et al., 2017) and Resolution (Table 5; Digital Appendix A3). (A) As in epidote. (B) Sb in epidote. (C) Pb in epidote. (D) Mn in epidote. (E) Yb in epidote. Abbreviations: epi = epidote; m/m = metamorphic; Res = Resolution.

Figure 18: As-Sb data cloud of epidote LA-ICP-MS data from selected giant and small porphyry copper deposits (gray circles). Also shown are epidote data from the Resolution blind test (red circles) and metamorphic epidote (blue circles). Resolution epidote has As and Sb contents consistent either with proximity to a giant porphyry deposit, or distal to a small porphyry. Abbreviation: PCDs — porphyry copper deposits. Data sources: El Teniente from

Wilkinson et al. (this volume), Quebrada Blanca, Ujina, and Rosario from Baker et al. (this volume), Batu Hijau — Wilkinson et al. (2015); Black Mountain from Cooke et al. (2014); Endeavour 48 and Endeavour 26 from Pacey et al. (this volume a), metamorphic epidote from Baker et al. (2017); Resolution (Table 5; Digital Appendix A3).

Figure 19: Calculated distances to the center of the porphyry system in the Resolution blind test based on LA-ICP-MS analyses of chlorite and application of the Batu Hijau Ti/Sr proximator (Wilkinson et al., 2015). X = distance to deposit center. Samples with no chlorite data are shown with a 'x' symbol. The calculated distances from each sample are shown as a dashed circle with the same color as the sample point. The proximator results converge on an area between the two sample clusters, with spatial coordinates centered on 4,683,375 m N and 494,300 m E, as highlighted by the large red circle—this is the predicted drill target from the Resolution blind test.

Figure 20: Results of the Resolution blind test plotted on section 494,300 m E together with drill hole and sample locations, the outline of the 1 % Cu shell, alteration domains as mapped by Resolution Copper Mining and the drill target from the chlorite proximator (large red circle) as shown in Figure 19. Cross-section provided courtesy of Rio Tinto Exploration. Abbreviations: AA = advanced argillic alteration; carb = carbonate; chl = chlorite; epi = epidote; QSP = quartz-sericite-pyrite alteration.

Table Captions

Table 1: Major element data (wt %) for drill core samples from Resolution. Full results are provided in Digital Appendix A1.

UTM coordinate system: WGS 84, UTM 12N. Abbreviations: DDH = diamond drillhole; Elev = elevation; Kvs = Cretaceous volcanoclastic rock; pC = Proterozoic dolerite.

Table 2: Trace element data (ppm) for drill core samples from Resolution. Full results are provided in Digital Appendix A1.

UTM coordinate system: WGS 84, UTM 12N. Abbreviations: DDH = diamond drillhole; East = easting; Elev = elevation; Kvs = Cretaceous volcanoclastic rock; North = northing; pC = Proterozoic dolerite.

Table 3: Results of K-feldspar staining and SWIR analyses of drill core samples from Resolution.

Abbreviations: DDH = diamond drillhole; Kvs = Cretaceous volcanoclastic rock.

Table 4: Summary of major and trace element LA-ICP-MS spot analyses of pyrite from the Resolution porphyry Cu-Mo deposit. Minimum and maximum values and the number of analyses from each sample are provided. Calculated radial distances to the center of the porphyry deposit are also provided. All data listed in Digital Appendix A2.

Abbreviations: BDL = Below detection limit; PCD = porphyry copper deposit; No. = number.

Table 5: Summary of trace element LA-ICP-MS spot analyses of epidote from Resolution. Minimum and maximum values and the number of analyses from each sample are provided. Calculated radial distances to the center of the porphyry deposit are also provided. All data listed in Digital Appendix A3.

Abbreviations: BDL = Below detection limit; PCD = porphyry copper deposit; No. = number.

Table 6: Summary of major and trace element LA-ICP-MS spot analyses of chlorite from Resolution. Minimum and maximum values and the number of analyses from each sample are provided. Calculated radial distances to the center of the porphyry deposit are also provided. All data listed in Digital Appendix A4.

Abbreviations: BDL = Below detection limit; PCD = porphyry copper deposit; No. = number.

Appendices

Digital Appendix A: Geochemical data from Resolution. (A1) Whole rock geochemical analyses. (A2) LA-ICP-MS spot analyses of pyrite. (A3) LA-ICP-MS spot analyses of epidote. (A4) LA-ICP-MS spot analyses of chlorite.

Digital Appendix B: LA-ICP-MS maps of mineral grains from Resolution. (B1) LA-ICP-MS maps of pyrite from samples (A) 10046359 and (B) 10046361. (B2) LA-ICP-MS maps of epidote from samples (A) 10046353, (B) and (C) 10046359. (B3) LA-ICP-MS map of chlorite from sample 10046359.

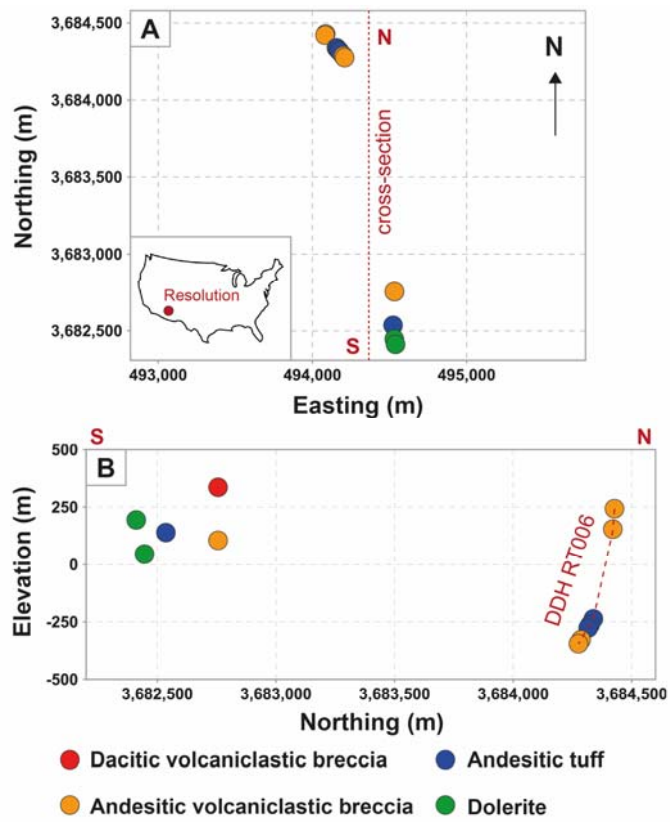


Figure 1

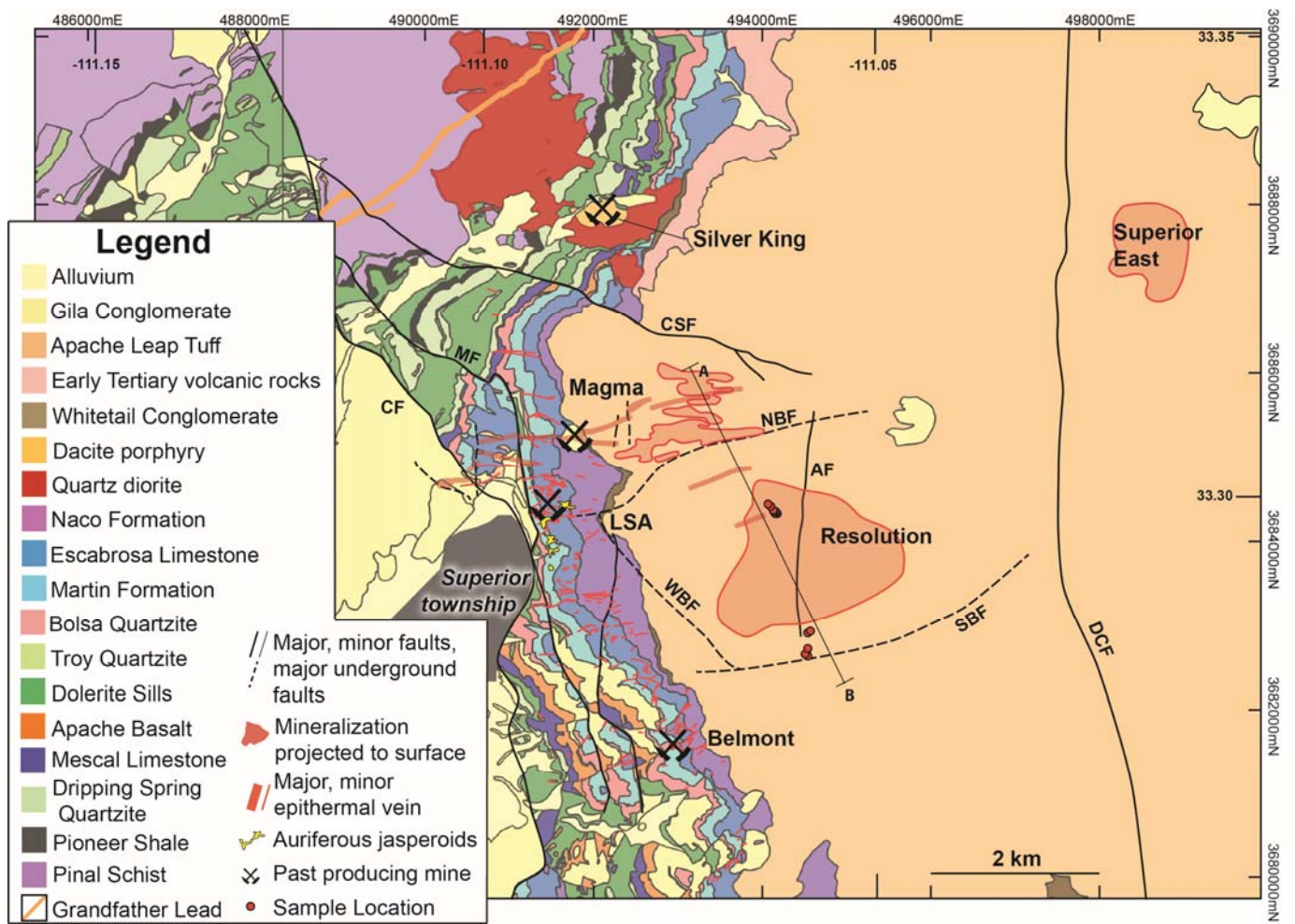


Figure 2

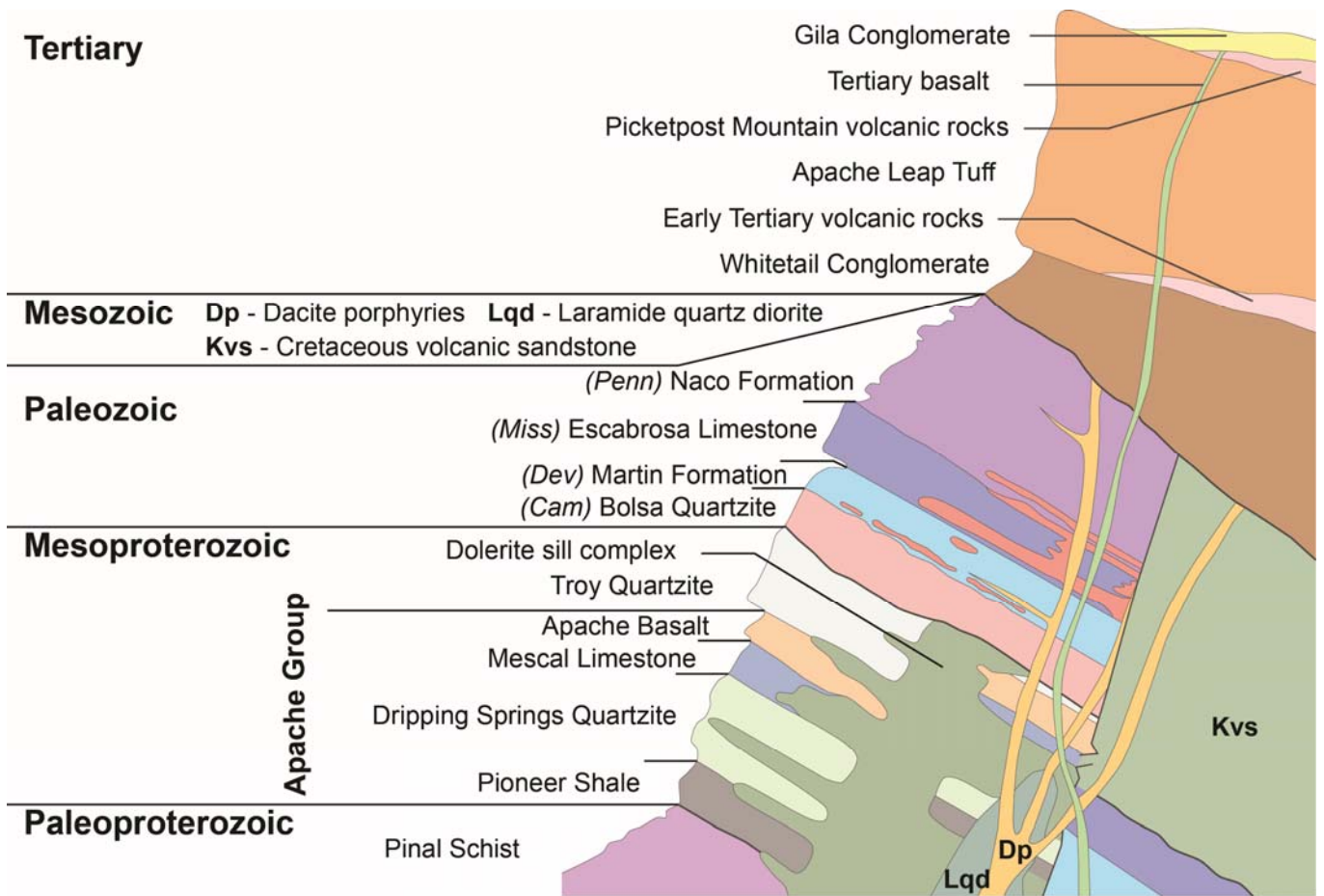


Figure 3

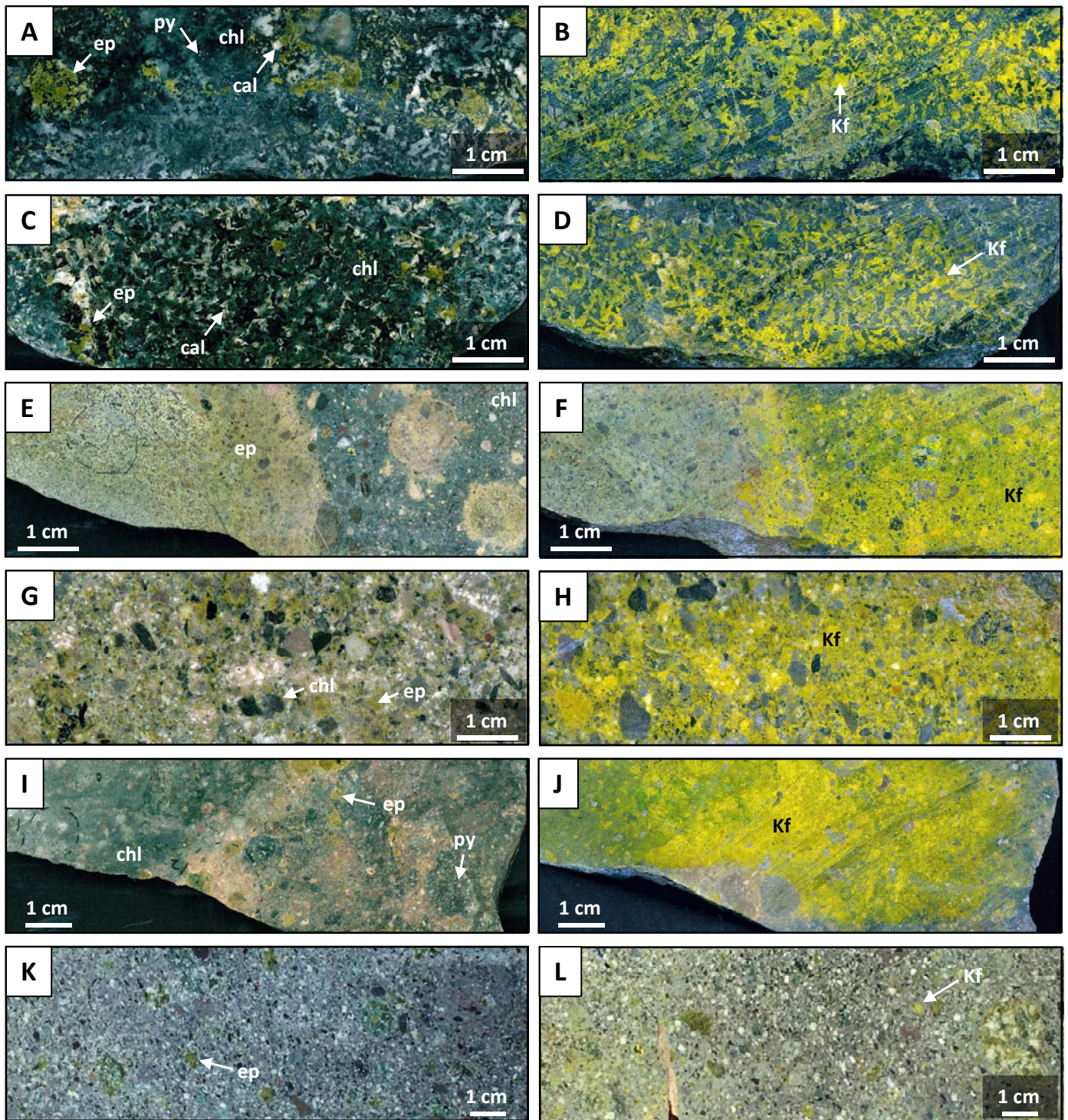


Figure 4

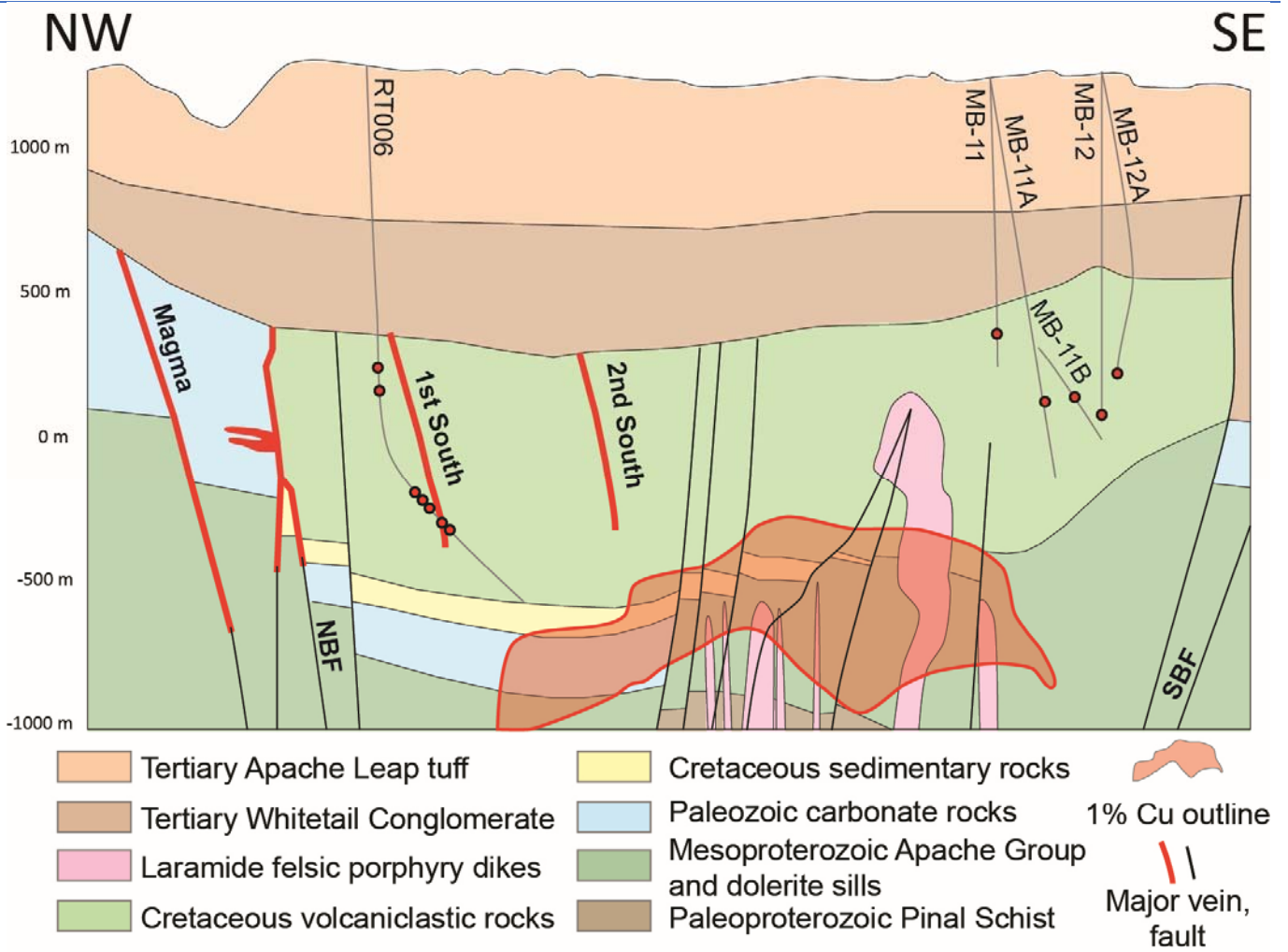


Figure 5

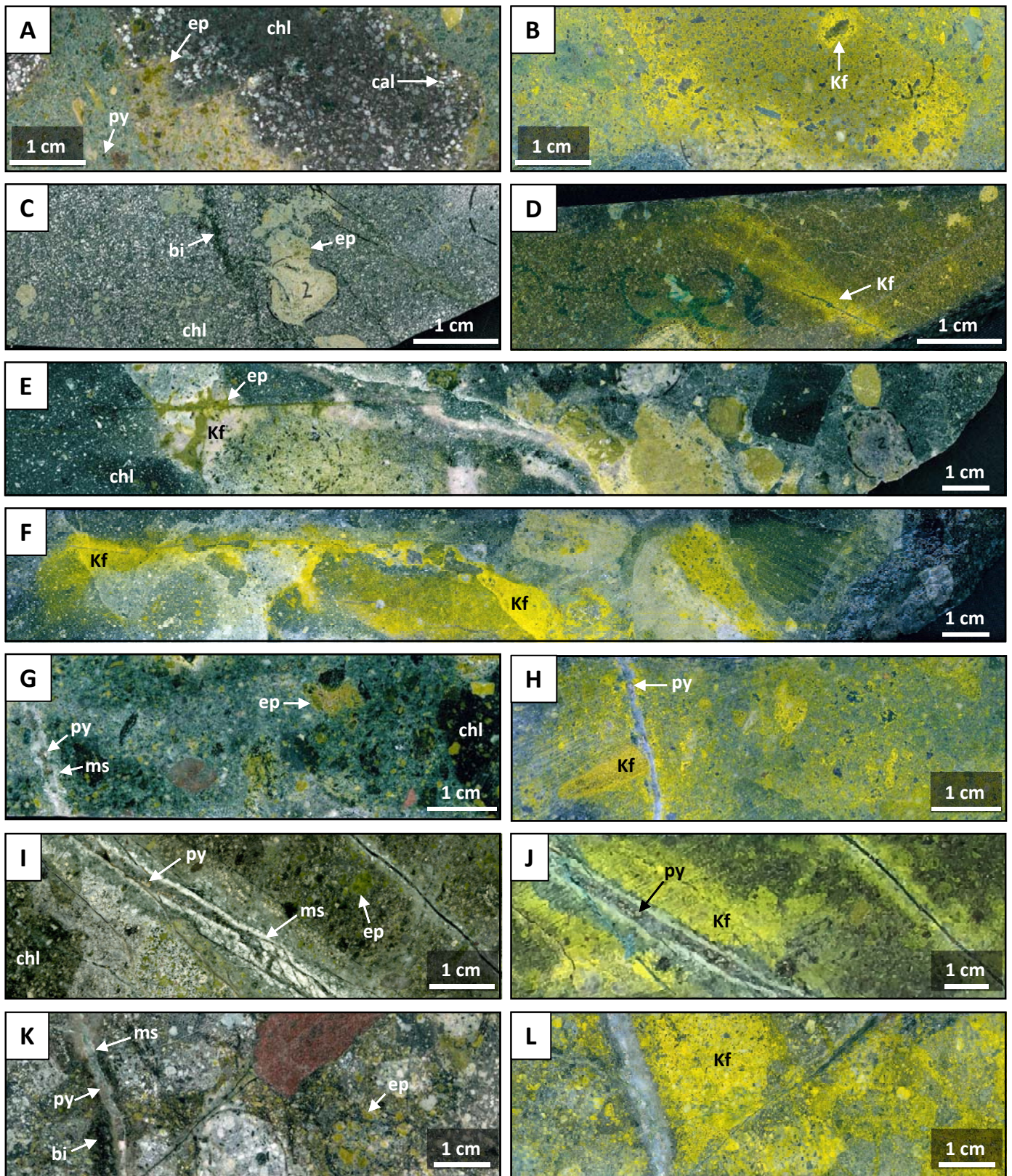


Figure 6

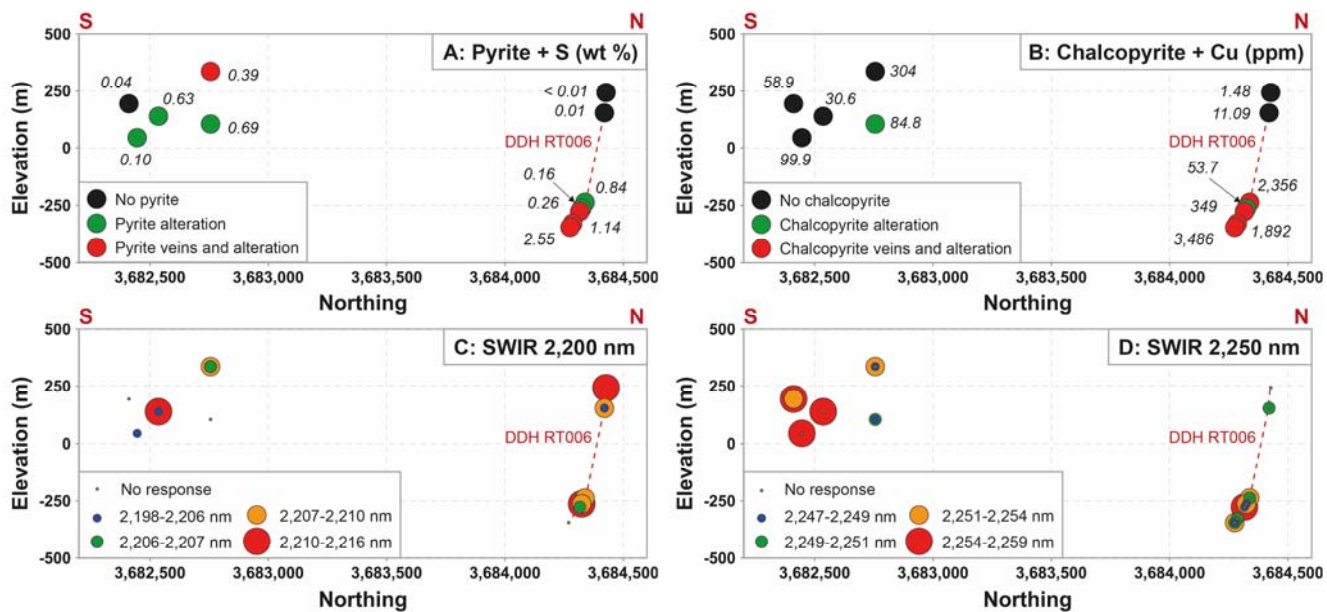


Figure 7

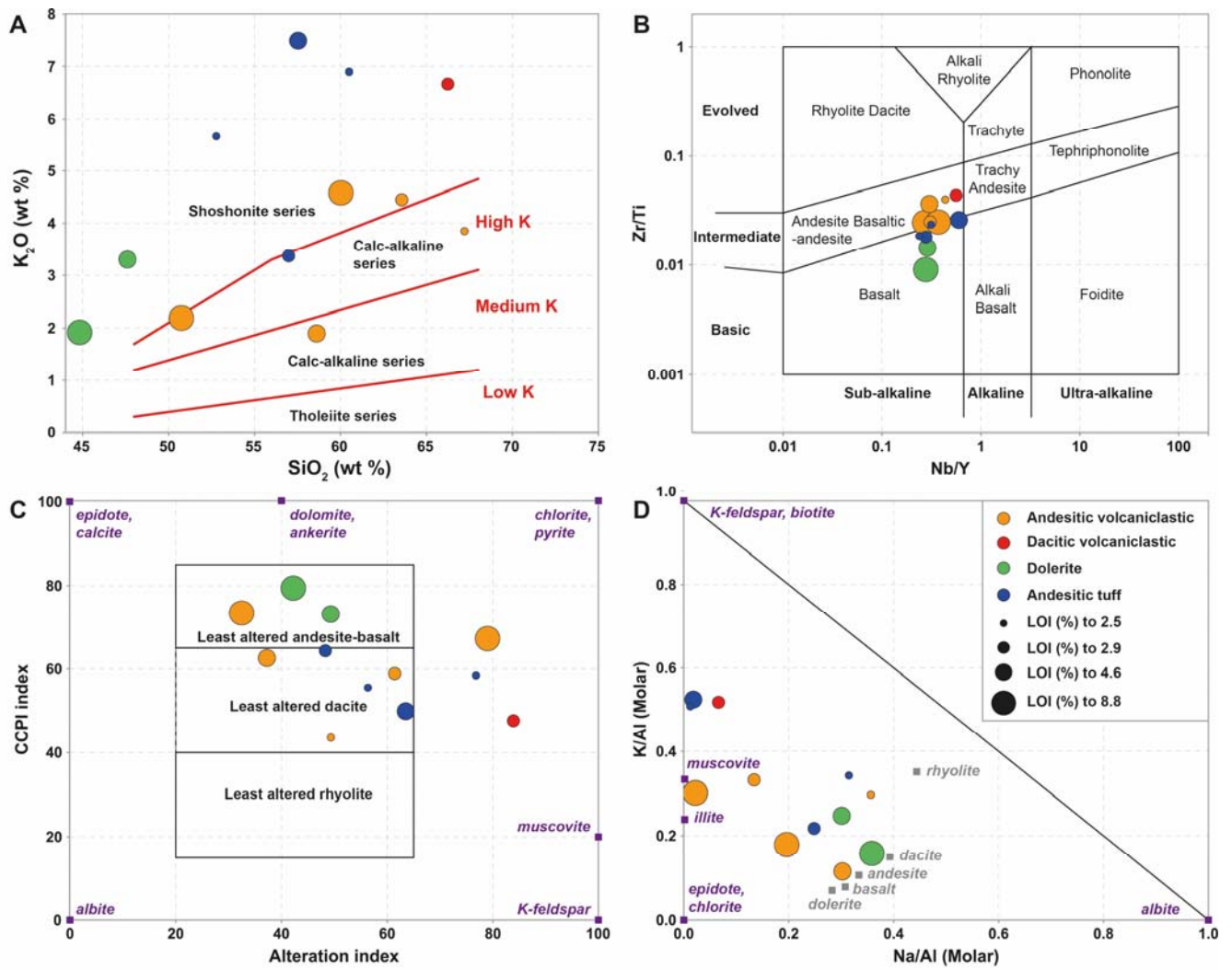


Figure 8

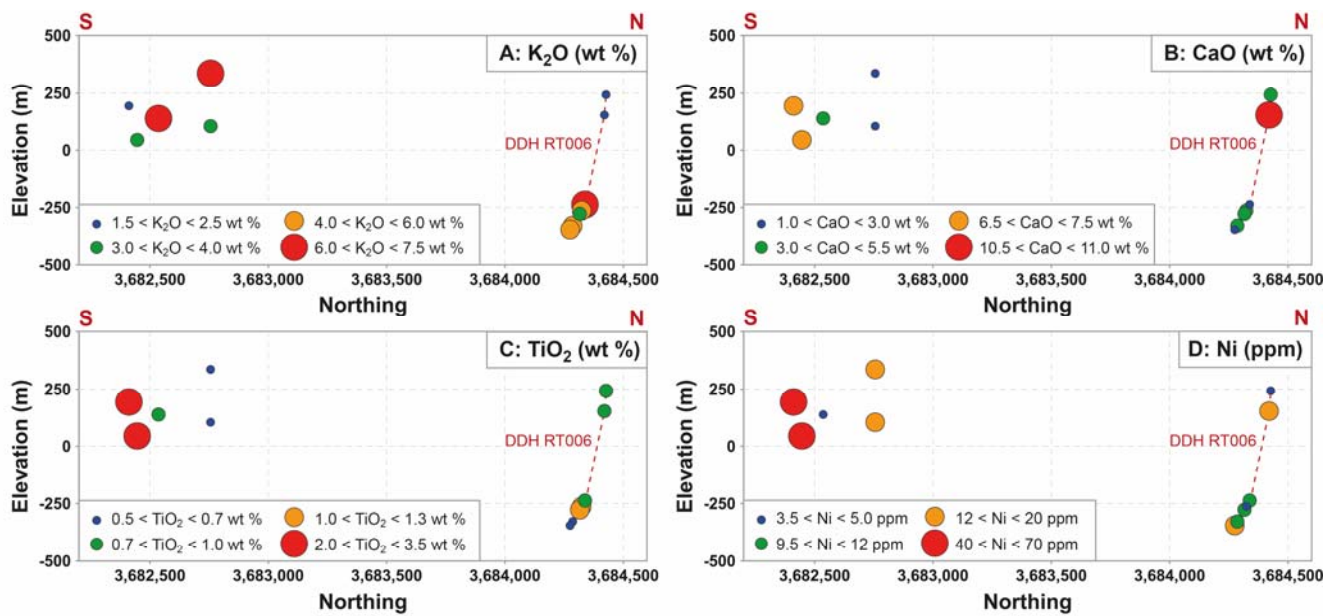


Figure 9

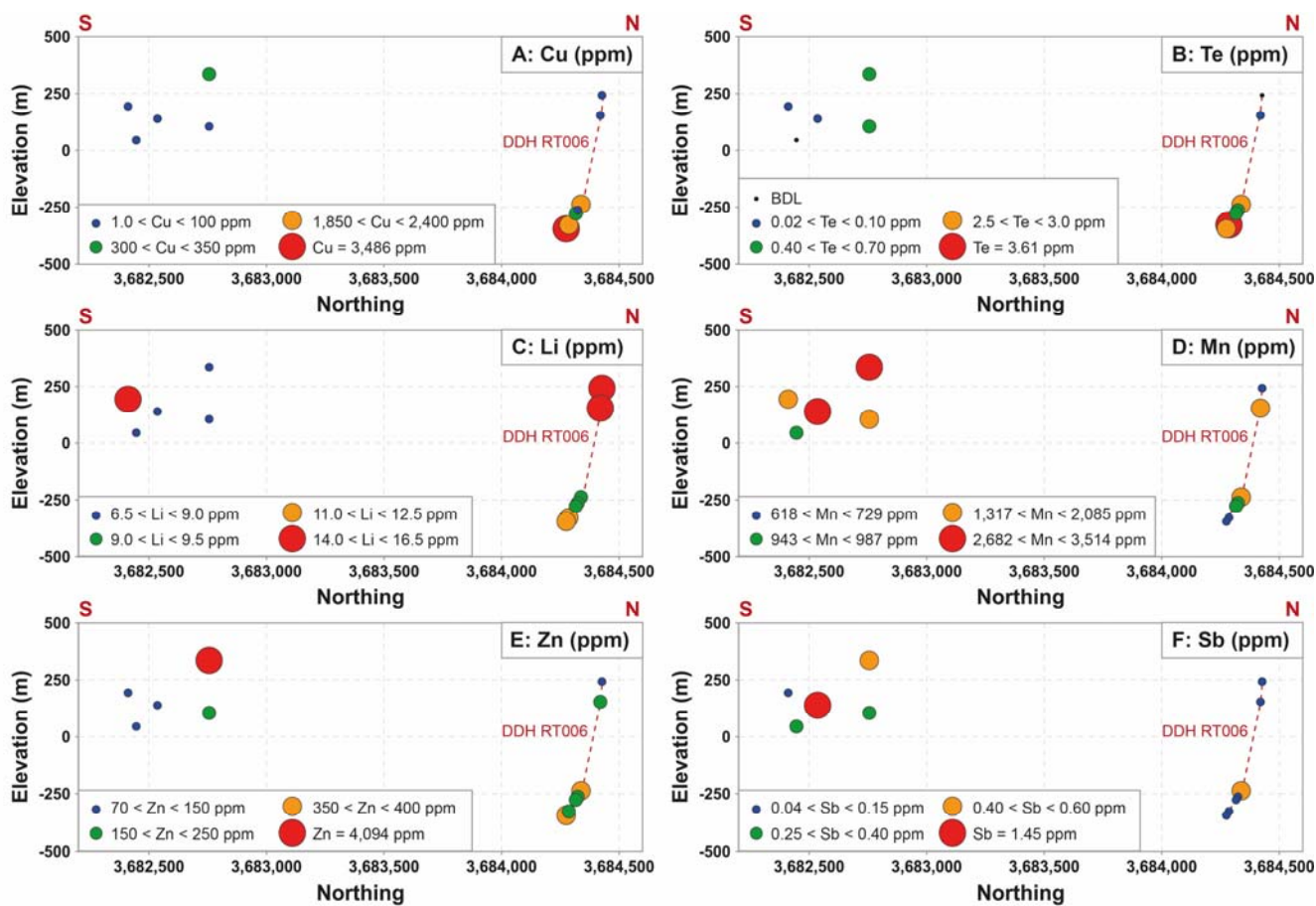


Figure 10

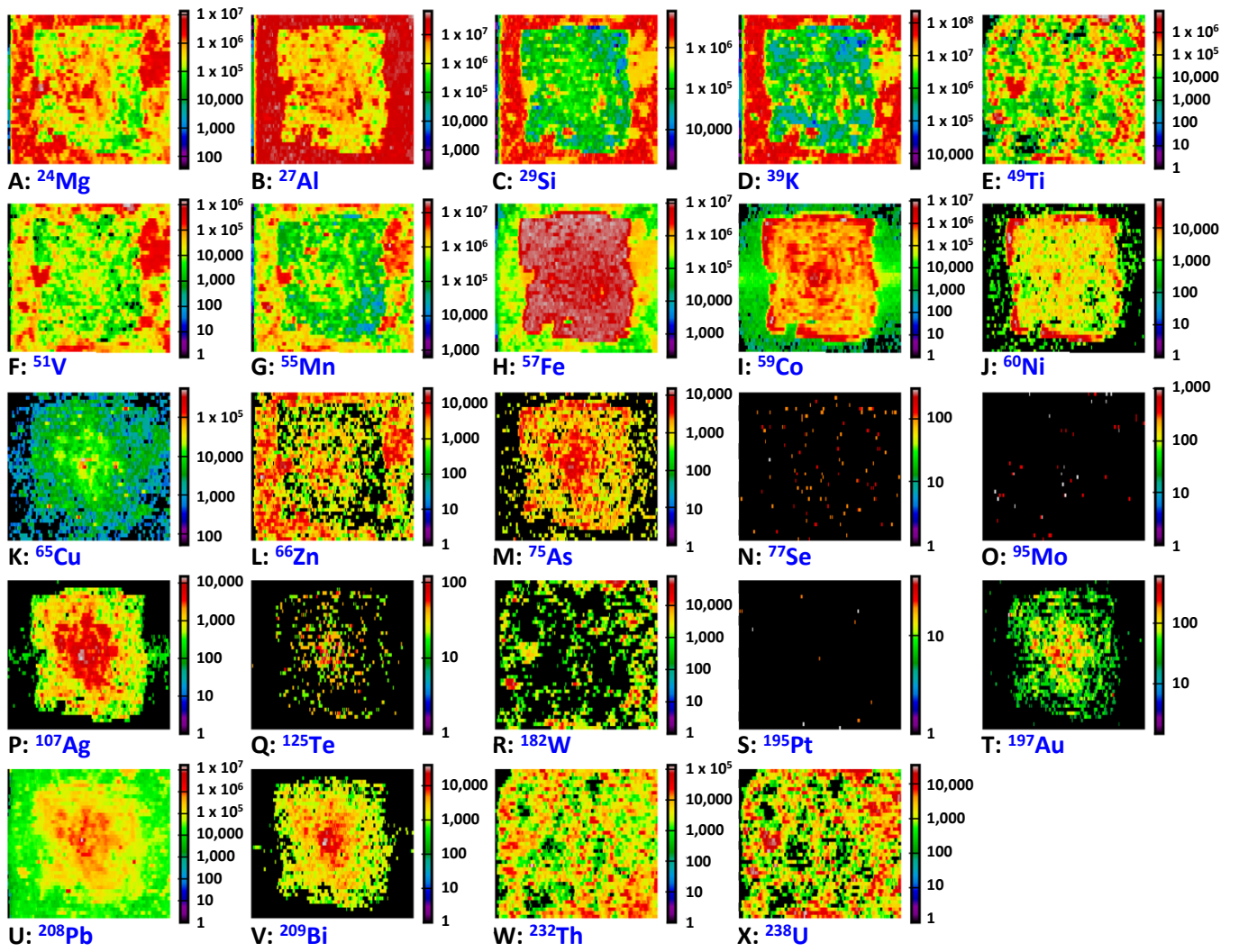


Figure 11

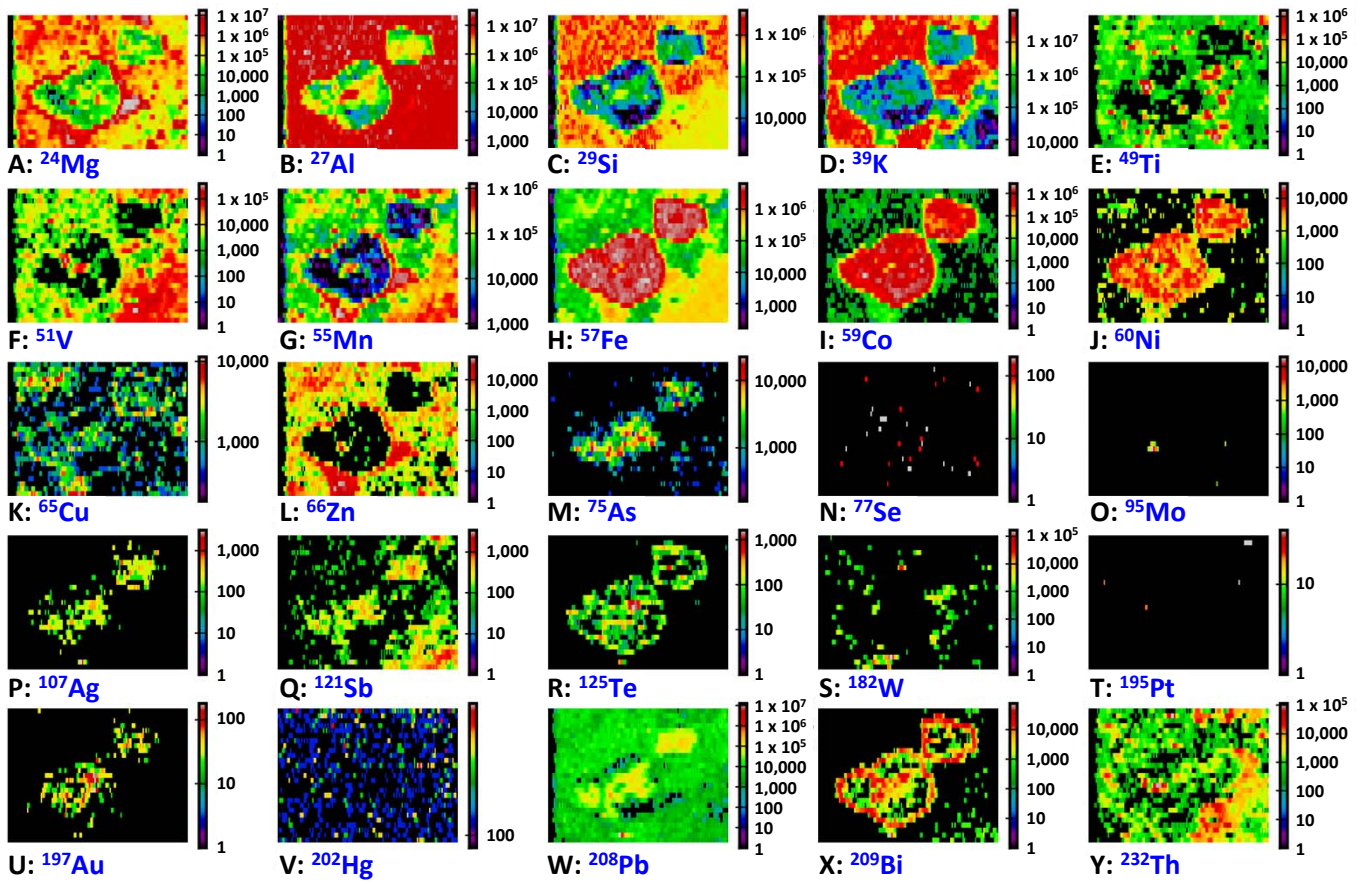


Figure 12

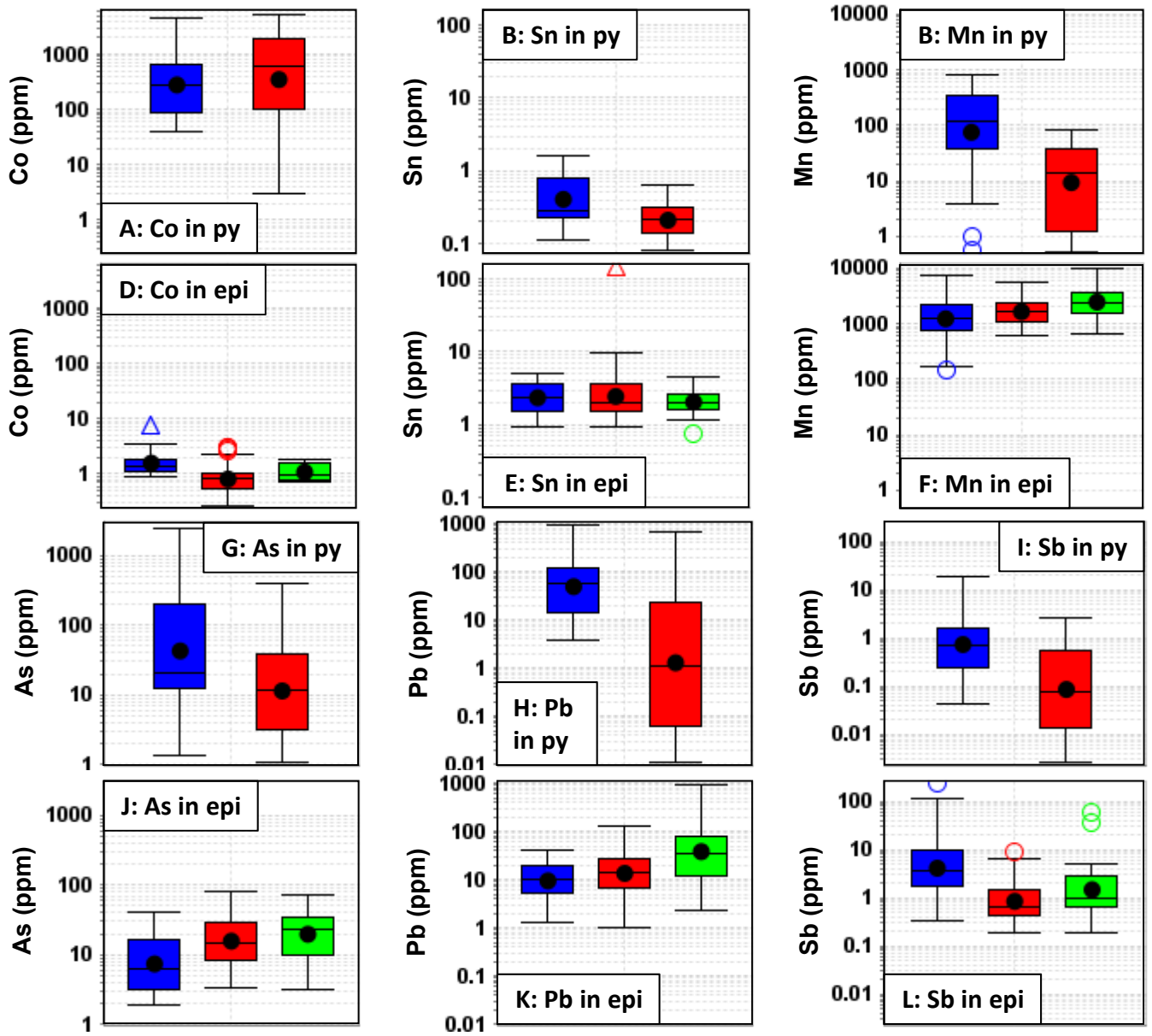


Figure 13

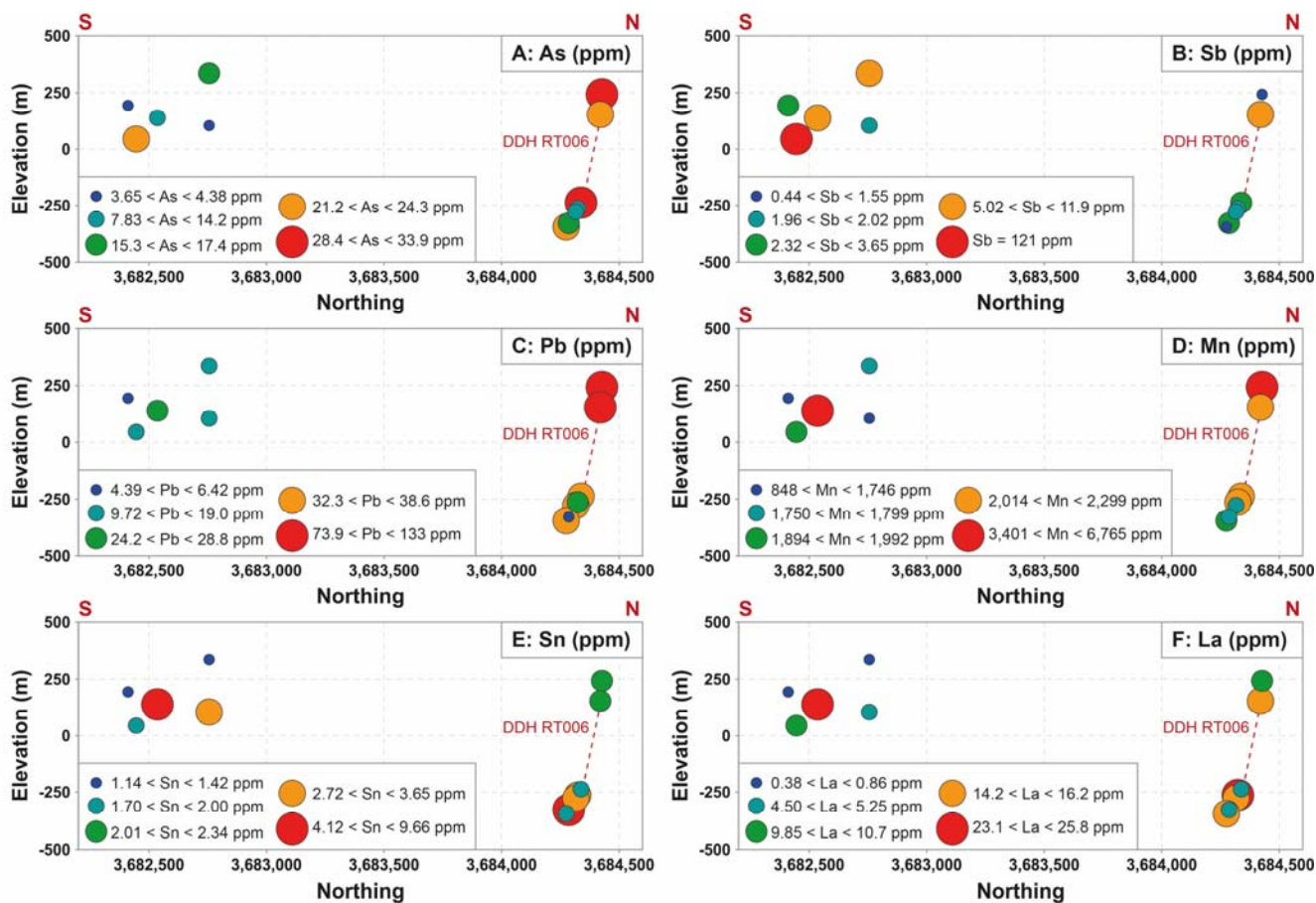


Figure 14

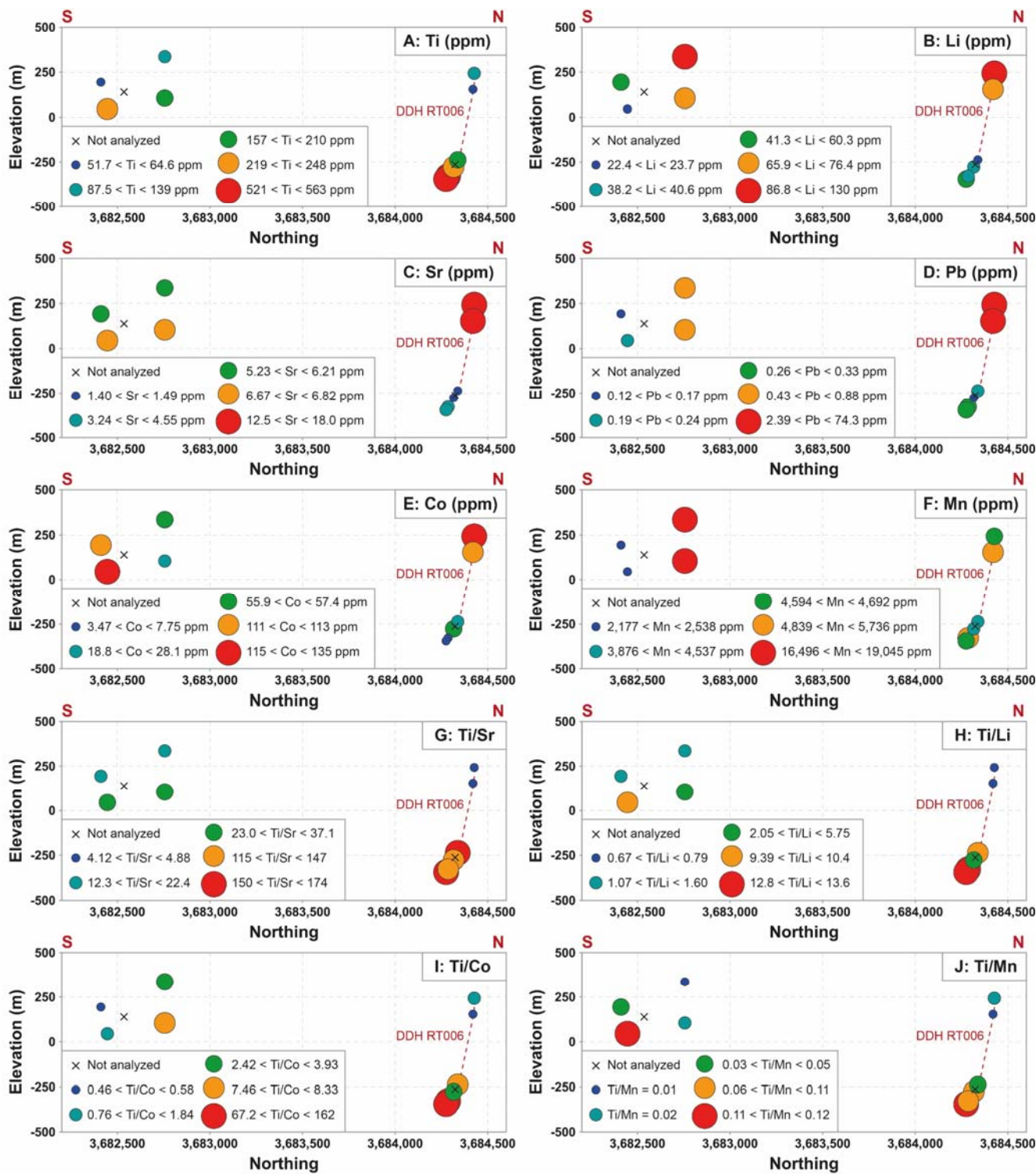


Figure 15

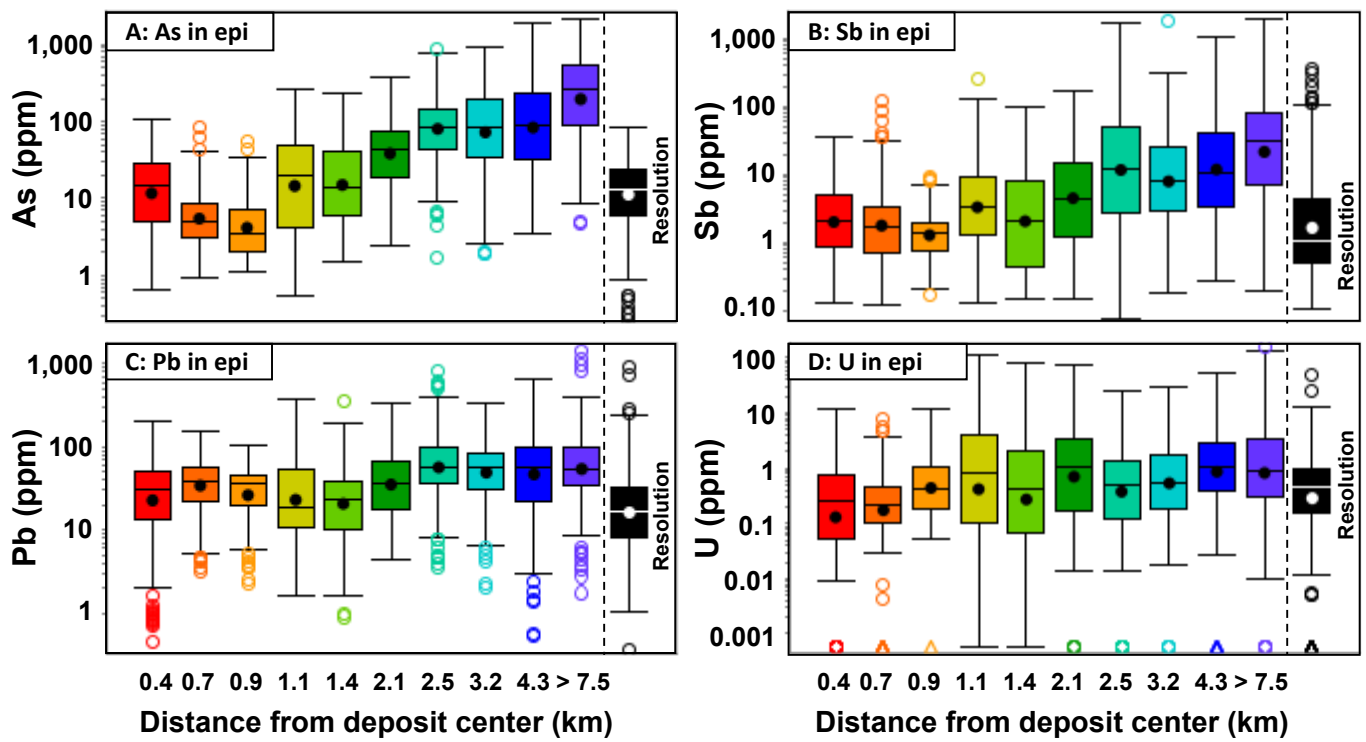


Figure 16

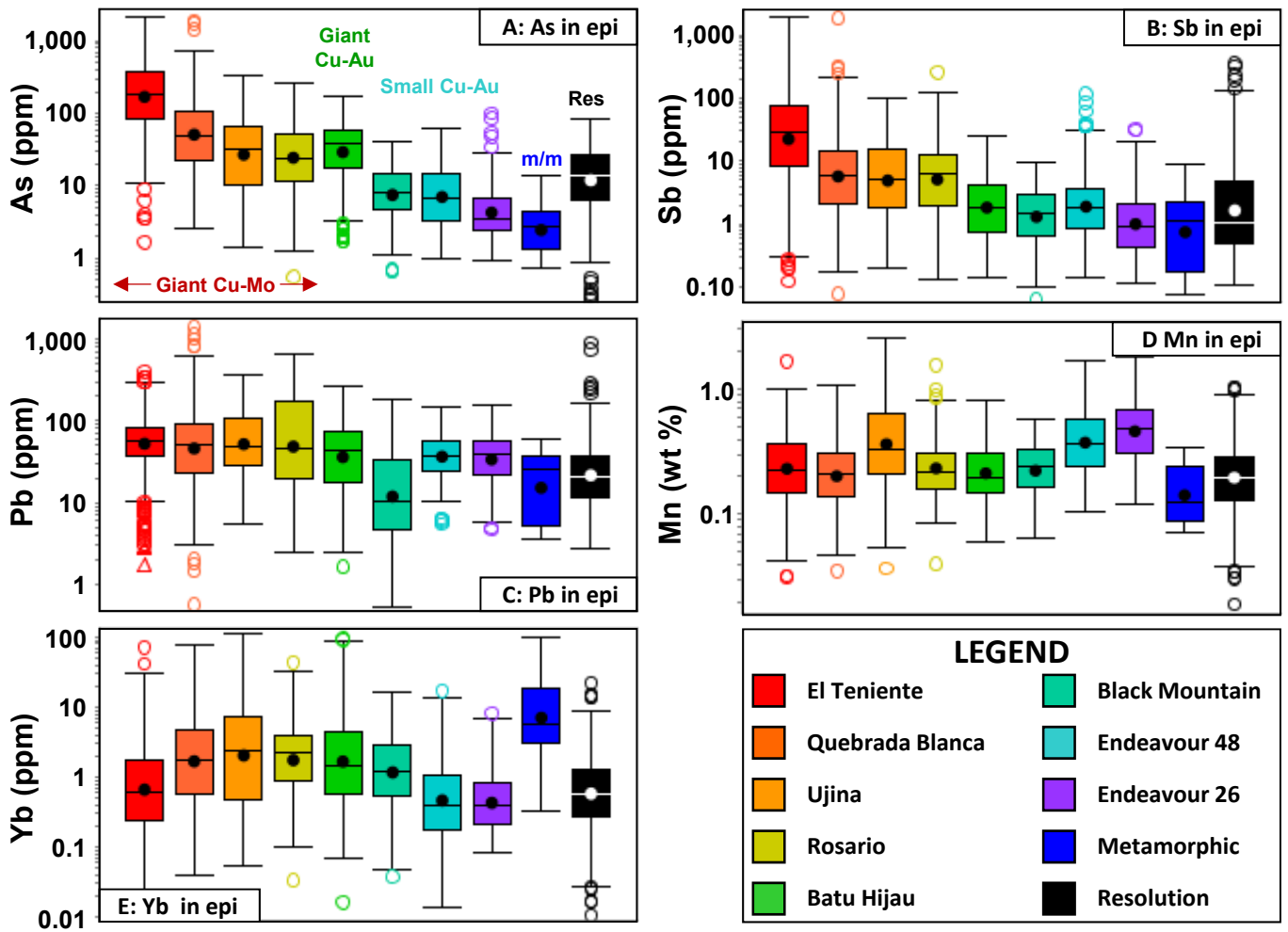


Figure 17

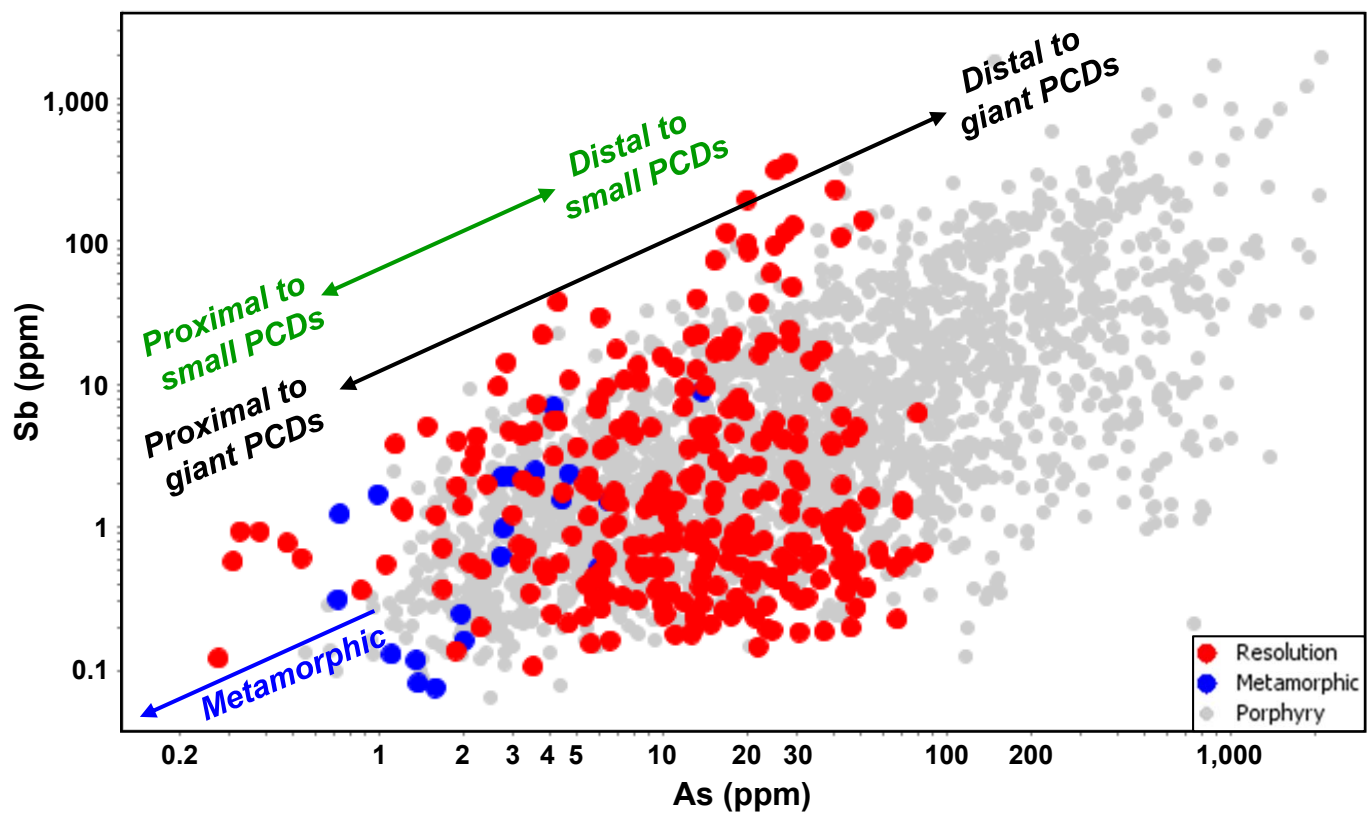


Figure 18

Chlorite – Ti / Sr proximator results

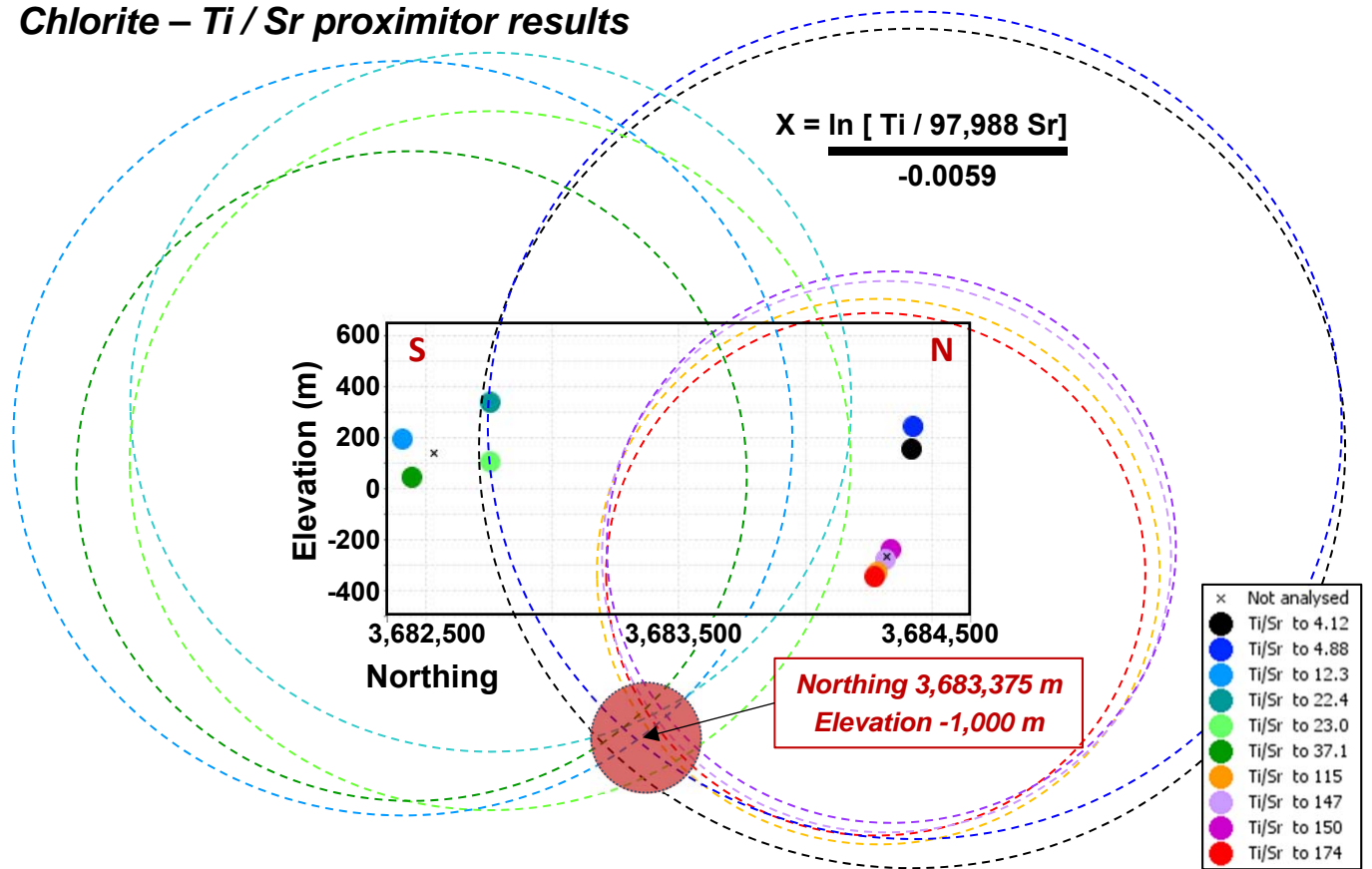


Figure 19

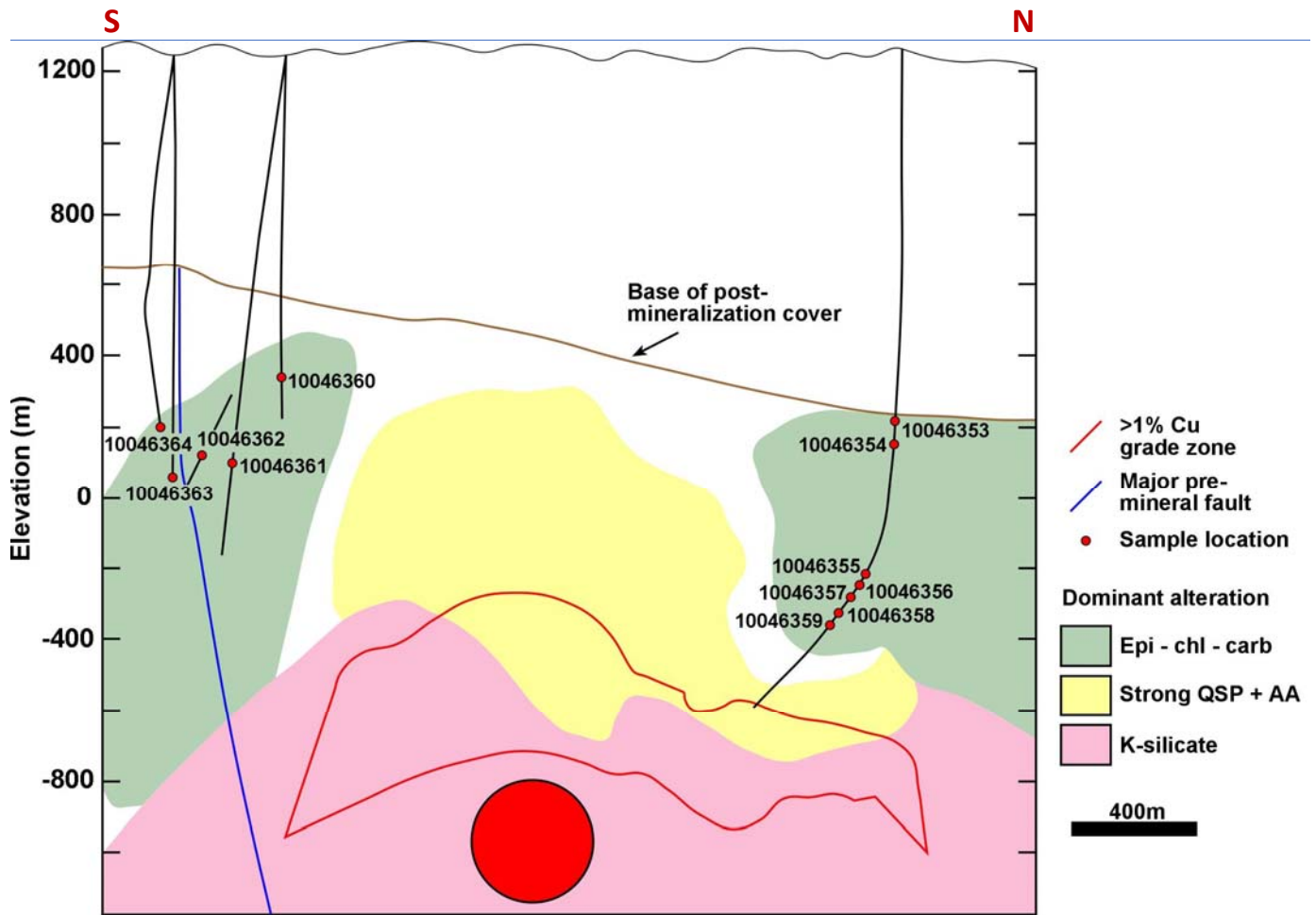


Figure 20

Table 1 – Major element data (wt %) for drillcore samples from Resolution. Full results are provided in Digital Appendix A1.

Sample	1004 6353	1004 6354	1004 6355	1004 6356	1004 6357	1004 6358	1004 6359	1004 6360	1004 6361	1004 6362	1004 6363	1004 6364
DDH	RT006	MB-11	MB-11A	MB-11B	MB-12	MB-12A						
Depth (m)	1,018	1,104	1,520	1,551	1,571	1,634	1,656	906	1,148	1,137	1,206	1,068
Easting	494086	494082	494156	494169	494176	494201	494209	494532	494532	494523	494531	494539
Northing	3684427	3684420	3684338	3684324	3684316	3684286	3684275	3682756	3682756	3682536	3682446	3682411
Elev (m)	243	154	-237	-263	-277	-328	-345	336	105	139	45	194
Unit	Kvs	pC	pC									
Major elements (wt %)												
SiO₂	58.61	50.74	60.50	52.77	56.98	63.56	60.02	66.24	67.21	57.53	47.60	44.82
Al₂O₃	17.90	13.25	14.69	17.88	16.76	14.49	16.44	13.93	14.03	15.45	14.43	13.17
Fe₂O₃	6.57	7.33	7.92	8.21	8.15	5.87	7.48	5.19	3.93	6.67	11.26	14.43
MgO	2.77	3.82	2.73	3.97	3.30	2.79	3.12	1.91	1.78	1.64	6.05	5.51
CaO	4.58	10.92	2.80	4.04	4.61	3.37	1.83	1.09	2.74	5.08	6.97	7.29
Na₂O	3.29	1.58	0.11	3.42	2.53	1.18	0.22	0.56	3.04	0.17	2.64	2.87
K₂O	1.90	2.19	6.90	5.66	3.37	4.45	4.58	6.67	3.85	7.49	3.30	1.92
TiO₂	0.75	0.73	0.83	1.14	0.98	0.61	0.65	0.53	0.53	0.85	2.12	3.42
P₂O₅	0.22	0.16	0.28	0.29	0.22	0.17	0.20	0.13	0.13	0.30	0.36	0.50
MnO	0.12	0.23	0.19	0.14	0.17	0.11	0.11	0.38	0.28	0.49	0.32	0.48
Cr₂O₃	<0.01	<0.01	<0.01	<0.01	<0.01	<0.01	<0.01	<0.01	<0.01	<0.01	<0.01	<0.01
LOI	3.1	8.8	2.5	2.2	2.6	2.9	4.7	2.6	2.2	4.1	4.6	5.3
Total C	0.05	1.66	0.06	0.05	0.03	0.04	0.04	0.12	0.15	0.52	0.68	0.78
Total S	<0.01	0.01	0.16	0.84	0.26	1.14	2.55	0.69	0.38	0.63	0.04	0.10

UTM coordinate system: WGS 84, UTM 12N. Abbreviations: DDH = diamond drillhole; Elev = elevation; Kvs = Cretaceous volcanoclastic rock; pC = Proterozoic dolerite.

Table 2 – Trace element data (ppm) for drillcore samples from Resolution. Full results are provided in Digital Appendix A1.

Sample	1004 6353	1004 6354	1004 6355	1004 6356	1004 6357	1004 6358	1004 6359	1004 6360	1004 6361	1004 6362	1004 6363	1004 6364
DDH	RT006	MB-11	MB-11A	MB-11B	MB-12	MB-12A						
Depth (m)	1,018	1,104	1,520	1,551	1,571	1,634	1,656	906	1,148	1,137	1,206	1,068
East	494086	494082	494156	494169	494176	494201	494209	494532	494532	494523	494531	494539
North	368442 7	3684420	3684338	3684324	3684316	3684286	3684275	368275 6	3682756	3682536	368244 6	368241 1
Elev (m)	243	154	-237	-263	-277	-328	-345	336	105	139	45	194
Unit	Kvs	pC	pC									
Trace elements (ppm)												
Ag	0.058	0.050	2.470	0.129	0.229	0.893	1.267	1.169	0.312	0.172	0.309	0.319
As	1.50	1.00	1.80	1.70	0.80	1.20	0.30	0.90	2.30	4.40	1.20	1.30
Au	0.0037	0.005	0.0272	0.0145	0.0098	0.0075	0.0125	0.006	0.0075	0.0032	<0.001	<0.001
Ba	285	384	433	435	776	575	414	853	590	981	310	194
Bi	0.03	<0.01	6.79	1.2	0.95	7.32	6.21	1.12	0.38	0.07	<0.01	<0.01
Cd	0.53	0.64	<0.02	0.06	0.06	0.16	0.12	16.52	0.47	0.13	0.04	0.29
Ce	56.7	32.3	41.4	44.0	33.8	31.7	33.8	41.6	48.2	51.9	33.9	44.3
Co	11.8	19.3	9.90	20.4	18.3	17.2	15.7	13.3	8.20	10.7	32.3	36.9
Cr	4.9	17.0	5.8	2.2	14.4	13.9	10.1	17.0	21.2	8.5	89.5	123.4
Cs	1.9	0.6	2.1	6.3	2.5	3.3	4.3	3.6	2.1	4.3	4.4	1.5
Cu	1.48	11.1	2,356	53.7	349.0	1,892	3,486	304.0	84.8	30.6	58.9	99.9
Eu	1.46	0.93	1.21	1.4	1.19	0.94	1.02	0.91	1.00	1.33	1.56	2.25
La	24.9	14.7	17.4	18.9	15.5	14.5	15.7	18.4	22.1	23.6	13.4	17.1
Li	16.1	14.7	9.3	9.4	9.3	11.1	12.1	8.0	7.2	8.6	6.7	16.4
Lu	0.40	0.27	0.29	0.36	0.27	0.20	0.23	0.24	0.24	0.29	0.45	0.53
Mn	618	1,639	1,317	943	948	666	729	2,682	1,942	3,514	987	2,085
Mo	0.21	0.26	0.23	0.26	0.31	0.39	0.18	0.66	0.69	0.38	0.67	0.60
Nb	8.5	5.4	6.0	6.4	5.2	4.6	5.6	7.7	6.9	11.4	8.9	10.6
Nd	28.1	18.3	23.0	25.3	18.3	16.0	18.6	19.5	21.9	25.4	20.9	29.4
Ni	4.7	14.3	9.9	3.7	11.4	11.6	13.2	18.5	16.4	4.9	67.2	44.8
Pb	10.0	50.7	6.42	6.01	3.64	5.32	6.84	532	33.3	40.5	3.86	15.4
Rb	77.0	63.6	167.8	239.0	102.1	148.1	175.4	191.6	106.9	212.0	93.2	48.7
Sb	0.05	0.13	0.46	0.11	0.10	0.07	0.06	0.55	0.35	1.45	0.27	0.10
Sc	13	14	13	19	17	10	11	8	7	12	25	43
Se	<0.1	0.2	0.2	0.2	0.1	0.4	1.4	0.4	0.1	<0.1	0.1	0.3
Sn	2.0	<0.2	4.0	2.0	4.0	4.0	10.0	1.0	2.0	1.0	1.0	2.0
Sr	451.4	308.8	148.0	394.1	470.7	286.5	110.0	179.9	333.8	229.6	314.3	221.5
Te	<0.05	0.02	2.77	0.62	0.43	3.61	2.80	0.70	0.48	0.07	<0.05	0.02
Tl	0.05	<0.02	0.17	0.90	0.28	0.47	0.34	0.11	0.07	0.14	0.28	<0.02
U	1.0	1.0	2.0	0.5	0.8	1.7	2.8	1.7	1.4	1.6	0.6	0.6
V	83	145	108	175	160	95	106	65	60	126	184	388
W	<1	0.6	79.0	3.8	4.8	16.1	43.9	11.3	3.9	5.5	1.0	4.3
Y	28.2	20.0	19.1	26.8	18.7	15.0	15.1	13.7	15.8	19.0	30.9	38.2
Yb	2.89	2.00	2.14	2.61	1.91	1.43	1.57	1.65	1.66	1.95	3.00	3.50
Zn	141	179	381	218	174	206	381	4,094	223	107	74.5	117
Zr	164	108	117	127	106	91.2	96.8	138	127	132	183	186

UTM coordinate system: WGS 84, UTM 12N. Abbreviations: DDH = diamond drillhole; East – easting; Elev = elevation; Kvs – Cretaceous volcanoclastic rock; North – northing; pC – Proterozoic dolerite.

Table 3 – Results of K-feldspar staining and SWIR analyses of drillcore samples from Resolution.

Sample	DDH	Drillhole depth (m)	Host rock	K-feldspar staining	Spot number	Minerals detected by SWIR analyses	2,200 nm feature position	2,250 nm feature position
10046353	RES 006	1017.91 – 1018.75	Kvs – andesitic conglomerate	Only rare K-feldspar crystals stained (primary?)	1	Epidote, chlorite, minor phengite	2,216	
					2	Chlorite, muscovite, phengite, epidote	2,212	
10046354	RES 006	1104.20 – 1105.09	Kvs – andesitic conglomerate	Intense K-feldspar alteration of large clast and moderate matrix alteration	1	Chlorite, muscovite	2,206	2,254
					2	Epidote, chlorite		2,250
					3	Montmorillonite	2,209	
10046355	RES 006	1519.67 – 1520.62	Kvs – andesitic tuff	Intense K-feldspar vein halo; patchy selective K-feldspar alteration	1	Chlorite, kaolinite		
					2	Epidote, trace muscovite	2,207	2,249
					3	Kaolinite, chlorite		2,253
10046356	RES 006	1551.37 – 1552.48	Kvs – andesitic tuff	Intense K-feldspar halo to epidote vein; selective K-feldspar alteration of matrix, clasts and clast rinds	1	Montmorillonite, chlorite	2,207	2,248
					2	Muscovite, chlorite	2,209	
					3	Montmorillonite, epidote	2,211	2,255
					4	Epidote, chlorite, minor muscovite and phengite	2,212	
10046357	RES 006	1570.85 – 1571.89	Kvs – andesitic tuff	Selectively pervasive; most intensely developed K-feldspar in matrix	1	Muscovite, chlorite	2,206	2,251
					2	Kaolinite, chlorite		
					3	Epidote		
10046358	RES 006	1634.31 – 1635.18	Kvs – reworked andesitic volcanics	Pervasive; most intense K-feldspar alteration outside the quartz – pyrite – muscovite vein halo	1	Muscovite, minor chlorite	2,210	2,250
					2	Muscovite, chlorite	2,206	
					3	Halloysite		2,248
10046359	RES 006	1656.03 – 1657.16	Kvs – reworked andesitic volcanics	Stockwork of K-feldspar stringer veins with thin K-feldspar halos – some clasts have been intensely altered to K-feldspar	A1	Halloysite		2,247
					A2	Halloysite, minor chlorite		2,251
					A3	Halloysite, trace chlorite		
					B1	Halloysite, minor chlorite		2,252
					B2	Halloysite, minor chlorite		2,248
B3	Chlorite, halloysite		2,251					
10046360	MB-11	905.84 – 907.18	Kvs – reworked dacitic volcanics	Intense, pervasive alteration of matrix; also rim of large clast altered to K-feldspar	1	Epidote, chlorite, montmorillonite	2,208	2,249
					2	Chlorite, montmorillonite	2,207	
					3	Chlorite, muscovite	2,207	2,256
10046361	MB-11A	1147.82 – 1149.92	Kvs – reworked andesitic volcanics	Intense, selective K-feldspar alteration of matrix and smaller clasts	1	Chlorite, montmorillonite	2,207	2,259
					2	Chlorite, montmorillonite	2,207	
10046362	MB-11B	1136.99 – 1138.00	Kvs – andesitic tuff	Intense, pervasive K-feldspar alteration of clasts and matrix	1	Muscovite, trace chlorite	2,206	2,254
					2	Epidote		
					3	Epidote, trace phengite	2,216	2,253
10046363	MB-12	1206.19 – 1206.83	Proterozoic dolerite	Selective K-feldspar alteration of plagioclase (moderate intensity)	1	Muscovite, trace chlorite	2,202	2,253
					2	Epidote		2,256
					3	<i>Low reflectance</i>		
10046364	MB-12A	1067.62 – 1068.23	Proterozoic dolerite	Selective K-feldspar alteration of plagioclase (moderate intensity)	1	Chlorite, montmorillonite	2,198	
					2	Epidote, montmorillonite	2,201	2,254
					3	Epidote, montmorillonite		2,250

Abbreviations: DDH = diamond drillhole; Kvs = Cretaceous volcanoclastic rock.

Table 4 – Summary of major and trace element LA-ICP-MS spot analyses of pyrite from Resolution. Minimum and maximum values and the number of analyses from each sample are provided. Calculated radial distances to the center of the porphyry deposit are also provided. All data listed in Digital Appendix A2.

Sample	Easting	Northing	Elevation (m)	Distance to PCD (m)	No. of analyses	Ag (ppm)	As (ppm)	Au (ppm)	Co (ppm)	Cu (ppm)
10046356	494169	3684324	-263	907	5	0.069 – 1.20	8.09 – 99.8	0.060 – 0.610	508 – 2,020	1.25 – 70.1
10046357	494176	3684316	-277	893	10	<i>BDL</i> – 1.42	<i>BDL</i> – 17.6	<i>BDL</i> – 0.057	18.5 – 2,180	<i>BDL</i> – 325
10046358	494201	3684286	-328	840	10	<i>BDL</i> – 3.16	<i>BDL</i> – 388	<i>BDL</i> – 0.184	161 – 5,090	<i>BDL</i> – 222
10046359	494209	3684275	-345	822	10	<i>BDL</i> – 0.107	<i>BDL</i> – 2.46	<i>BDL</i> – 0.002	2.58 – 179	0.288 – 45.6
10046360	494532	3682756	336	1,241	5	0.911 – 473	2.41 – 13.9	0.007 – 0.404	147 – 757	11.7 – 320
10046361	494532	3682756	105	1,077	8	0.523 – 14.4	163 – 2,600	0.018 – 0.482	41.7 – 316	2.90 – 157
10046362	494523	3682536	139	1,271	10	0.635 – 32.1	12.2 – 93.1	0.014 – 0.365	71.3 – 4,240	5.54 – 402

Sample	Mn (ppm)	Mo (ppm)	Ni (ppm)	Pb (ppm)	Sb (ppm)	Se (ppm)	Sn (ppm)	Te (ppm)	Tl (ppm)	Zn (ppm)
10046356	19.0 – 76.9	<i>BDL</i> – 0.107	1.33 – 6.85	3.01 – 53.9	0.095 – 1.30	<i>BDL</i> – 20.4	<i>BDL</i> – 0.655	35.5 – 162	<i>BDL</i> – 0.049	<i>BDL</i> – 70.5
10046357	<i>BDL</i> – 94.4	<i>BDL</i>	0.946 – 57.8	<i>BDL</i> – 28.6	<i>BDL</i> – 0.122	<i>BDL</i> – 6.00	0.244 – 0.423	0.900 – 37.8	<i>BDL</i> – 0.121	<i>BDL</i> – 13.2
10046358	<i>BDL</i> – 11.0	<i>BDL</i>	34.5 – 209	0.040 – 759	<i>BDL</i> – 2.86	<i>BDL</i> – 10.9	0.074 – 0.409	0.532 – 10,100	<i>BDL</i> – 0.139	0.428 – 8.34
10046359	<i>BDL</i> – 5.20	<i>BDL</i> – 0.121	2.39 – 130	<i>BDL</i> – 4.31	<i>BDL</i> – 0.042	6.64 – 71.1	0.112 – 0.291	<i>BDL</i> – 29.0	<i>BDL</i> – 0.021	<i>BDL</i> – 0.882
10046360	<i>BDL</i> – 104	<i>BDL</i> – 0.454	79.1 – 612	4.92 – 35.7	0.062 – 0.409	<i>BDL</i>	0.218 – 0.601	9.87 – 370	<i>BDL</i> – 0.078	0.403 – 11,005
10046361	4.46 – 788	<i>BDL</i> – 0.181	121 – 351	4.39 – 201	0.057 – 1.65	<i>BDL</i> – 1.12	0.107 – 2.70	40.0 – 123	<i>BDL</i> – 0.630	2.11 – 128
10046362	56.6 – 788	<i>BDL</i> – 0.410	4.63 – 170	24.4 – 889	0.770 – 19.1	<i>BDL</i> – 3.59	0.207 – 0.959	<i>BDL</i> – 2.76	0.027 – 0.798	1.12 – 21.1

Abbreviations: *BDL* = below detection limit; PCD = porphyry copper deposit; No. = number.

Table 5 – Summary of trace element LA-ICP-MS spot analyses of epidote from Resolution. Minimum and maximum values and the number of analyses from each sample are provided. Calculated radial distances to the center of the porphyry deposit are also provided. All data listed in Digital Appendix A3.

Sample	Easting	Northing	Elevation (m)	Distance to PCD (m)	No. of analyses	As (ppm)	Au (ppm)	Cu (ppm)	La (ppm)	Mg (ppm)	Mn (ppm)
10046353	494086	3684427	243	1,287	18	3.85 – 70.4	<i>BDL</i>	<i>BDL</i>	0.969 – 25.7	153 – 1,780	1,045 – 9,636
10046354	494082	3684420	154	1,227	14	3.13 – 58.3	<i>BDL</i> – 0.084	<i>BDL</i>	0.422 – 60.7	142 – 992	633 – 4,344
10046355	494156	3684338	-237	934	6	18.9 – 79.7	<i>BDL</i>	<i>BDL</i> – 4.73	0.390 – 10.8	695 – 2,410	854 – 3,760
10046356	494169	3684324	-263	907	16	5.75 – 39.5	<i>BDL</i>	<i>BDL</i> – 7.85	1.04 – 96.3	253 – 4,390	1,137 – 3,706
10046357	494176	3684316	-277	893	14	<i>BDL</i> – 45.9	<i>BDL</i>	<i>BDL</i> – 3.77	0.399 – 54.3	76.9 – 606	781 – 3,326
10046358	494201	3684286	-328	840	19	<i>BDL</i> – 83.0	<i>BDL</i>	<i>BDL</i> – 7.61	1.16 – 54.0	132 – 593	627 – 3,425
10046359	494209	3684275	-345	822	33	3.88 – 71.7	<i>BDL</i> – 0.010	<i>BDL</i> – 1.72	1.47 – 47.8	117 – 950	681 – 5,478
10046360	494532	3682756	336	1,241	7	5.52 – 33.4	<i>BDL</i>	<i>BDL</i> – 2.50	0.036 – 23.6	418 – 925	810 – 3,087
10046361	494532	3682756	105	1,077	11	<i>BDL</i> – 7.00	<i>BDL</i>	<i>BDL</i> – 21.9	0.270 – 15.2	179 – 864	432 – 4,303
10046362	494523	3682536	139	1,271	6	4.13 – 16.8	<i>BDL</i>	<i>BDL</i> – 5.78	5.74 – 64.1	468 – 3,830	5,665 – 7,539
10046363	494531	3682446	45	1,296	3	15.4 – 40.7	<i>BDL</i>	<i>BDL</i> – 1.48	0.451 – 27.5	<i>BDL</i> – 1,370	1,102 – 3,332
10046364	494539	3682411	194	1,405	21	<i>BDL</i> – 8.20	<i>BDL</i> – 0.095	<i>BDL</i>	<i>BDL</i> – 9.09	46.4 – 929	143 – 3,235

Sample	Mo (ppm)	Pb (ppm)	Sb (ppm)	Sr (ppm)	Sn (ppm)	Ti (ppm)	V (ppm)	Y (ppm)	Zn (ppm)	Zr (ppm)
10046353	<i>BDL</i> – 0.586	2.29 – 899	<i>BDL</i> – 5.21	124 – 2,010	<i>BDL</i> – 4.48	8.38 – 443	6.06 – 215	1.62 – 22.2	2.34 – 15.2	0.188 – 57.5
10046354	<i>BDL</i> – 0.371	11.6 – 284	<i>BDL</i> – 59.8	349 – 1,830	<i>BDL</i> – 4.21	26.3 – 684	7.85 – 399	0.103 – 43.9	2.95 – 20.3	<i>BDL</i> – 25.1
10046355	<i>BDL</i> – 0.540	22.5 – 81.5	0.534 – 6.30	202 – 471	<i>BDL</i> – 2.08	69.8 – 212	66.5 – 183	0.291 – 21.3	9.88 – 285	0.315 – 85.3
10046356	<i>BDL</i> – 0.236	4.48 – 70.8	<i>BDL</i> – 5.23	329 – 1,400	<i>BDL</i> – 6.21	65.1 – 622	22.5 – 757	0.136 – 123	6.13 – 145	<i>BDL</i> – 7.38
10046357	<i>BDL</i>	7.51 – 130	<i>BDL</i> – 9.40	560 – 2,910	<i>BDL</i> – 9.83	4.95 – 1,480	14.0 – 1,000	0.231 – 143	1.92 – 31.1	<i>BDL</i> – 26.3
10046358	<i>BDL</i> – 0.317	<i>BDL</i> – 20.4	<i>BDL</i> – 5.56	194 – 1,280	<i>BDL</i> – 144	2.90 – 992	0.637 – 590	0.097 – 62.8	<i>BDL</i> – 52.3	<i>BDL</i> – 19.0
10046359	<i>BDL</i> – 0.288	2.84 – 68.8	<i>BDL</i> – 1.26	285 – 2,500	<i>BDL</i> – 5.69	15.2 – 384	25.0 – 512	0.423 – 33.3	1.34 – 70.2	<i>BDL</i> – 21.5
10046360	<i>BDL</i> – 0.149	10.2 – 26.8	1.53 – 19.9	487 – 1,300	<i>BDL</i> – 3.50	<i>BDL</i> – 135	42.2 – 300	0.074 – 24.7	3.74 – 13.1	<i>BDL</i> – 0.810
10046361	<i>BDL</i>	2.98 – 20.1	<i>BDL</i> – 3.68	170 – 1,950	0.942 – 4.43	13.0 – 812	14.9 – 166	0.175 – 15.5	3.35 – 13.9	<i>BDL</i> – 5.20
10046362	<i>BDL</i> – 2.08	19.3 – 39.7	5.52 – 17.1	643 – 1,090	<i>BDL</i> – 5.07	101 – 584	268 – 735	4.67 – 45.1	8.51 – 36.5	0.154 – 41.9
10046363	<i>BDL</i>	16.5 – 22.0	16.8 – 232	859 – 1,280	<i>BDL</i> – 1.87	39.4 – 414	138 – 187	1.32 – 30.6	5.93 – 17.2	0.174 – 2.60
10046364	<i>BDL</i> – 0.198	1.29 – 17.7	<i>BDL</i> – 13.6	471 – 1,950	<i>BDL</i> – 1.30	<i>BDL</i> – 323	8.87 – 338	0.051 – 27.5	<i>BDL</i> – 7.07	<i>BDL</i> – 1.56

Abbreviations: *BDL* = below detection limit; PCD = porphyry copper deposit; No. = number.

Table 6 – Summary of major and trace element LA-ICP-MS spot analyses of chlorite from Resolution. Minimum and maximum values and the number of analyses from each sample are provided. Calculated radial distances to the center of the porphyry deposit are also provided. All data listed in Digital Appendix A4.

Sample	Easting	Northing	Elevation (m)	Distance to PCD (m)	No. of analyses	Al (wt %)	As (ppm)	B (ppm)	Ba (ppm)	Co (ppm)	Cr (ppm)	Cu (ppm)	Fe (wt %)	La (ppm)	
10046353	494086	3684427	243	1018	11	10.1 – 10.9	<i>BDL</i>	<i>BDL</i> – 20.5	<i>BDL</i> – 7.32	100 – 124	<i>BDL</i> – 124	2.26 – 28.4	21.1 – 25.3	<i>BDL</i> – 0.229	
10046354	494082	3684420	154	1104	13	10.1 – 10.5	<i>BDL</i>	<i>BDL</i> – 8.53	1.85 – 7.48	95.3 – 130	<i>BDL</i> – 5.69	44.7 – 113	21.9 – 26.4	<i>BDL</i> – 0.223	
10046357	494176	3684316	-277	1571	11	10.1 – 10.7	<i>BDL</i> – 1.23	<i>BDL</i> – 6.60	0.963 – 2.66	26.1 – 56.9	<i>BDL</i> – 55.0	<i>BDL</i> – 1.06	14.2 – 21.7	<i>BDL</i>	
10046358	494201	3684286	-328	1634	4	10.7 – 11.2	<i>BDL</i>	<i>BDL</i> – 5.36	1.10 – 6.17	6.03 – 10.2	14.5 – 43.9	0.780 – 1.60	15.9 – 16.8	<i>BDL</i> – 0.272	
10046359	494209	3684275	-345	1656	16	10.6 – 11.3	<i>BDL</i>	<i>BDL</i> – 7.91	<i>BDL</i> – 4.86	3.57 – 63.2	11.3 – 70.2	<i>BDL</i> – 5.91	14.4 – 17.9	<i>BDL</i> – 0.035	
10046360	494532	3682756	336	906	3	10.9	<i>BDL</i>	<i>BDL</i>	14.1 – 15.8	53.4 – 60.1	23.7 – 24.8	<i>BDL</i> – 3.54	15.1 – 15.9	<i>BDL</i> – 0.179	
10046361	494532	3682756	105	1148	6	10.2 – 10.5	<i>BDL</i> – 1.33	<i>BDL</i>	11.9 – 31.9	14.9 – 35.3	<i>BDL</i> – 94.1	<i>BDL</i> – 1.50	13.7 – 16.3	<i>BDL</i> – 0.036	
10046363	494531	3682446	45	1206	2	9.19	<i>BDL</i>	<i>BDL</i>	3.25 – 5.00	138 – 142	3.11 – 3.90	<i>BDL</i>	23.4 – 24.1	<i>BDL</i>	
10046364	494539	3682411	194	1068	16	9.22 – 9.46	<i>BDL</i> – 2.12	<i>BDL</i> – 8.70	<i>BDL</i> – 3.21	93.9 – 121	<i>BDL</i> – 120	<i>BDL</i> – 1.60	27.0 – 32.1	<i>BDL</i> – 0.290	
Sample	Li (ppm)	Mg (wt %)	Mn (wt %)	Na (ppm)	Ni (ppm)	Pb (ppm)	Sb (ppm)	Si (wt %)	Sn (ppm)	Sr (ppm)	Ti (ppm)	V (ppm)	Y (ppm)	Zn (ppm)	Zr (ppm)
10046353	<i>BDL</i> – 147	12.5 – 15.1	0.426 – 0.490	70.5 – 438	30.1 – 47.7	<i>BDL</i> – 4.11	<i>BDL</i>	13.7 – 16.7	<i>BDL</i> – 2.80	<i>BDL</i> – 32.7	<i>BDL</i> – 233	44.7 – 104	<i>BDL</i> – 0.219	922 – 1,740	<i>BDL</i> – 1.18
10046354	56.3 – 75.9	11.6 – 12.7	0.544 – 0.611	60.9 – 437	35.9 – 95.1	49.3 – 105	<i>BDL</i> – 0.204	12.9 – 18.4	<i>BDL</i> – 2.14	4.06 – 19.4	41.4 – 64.2	130 – 217	<i>BDL</i> – 0.408	1,900 – 3,130	<i>BDL</i> – 1.95
10046357	19.9 – 40.3	13.0 – 14.4	0.387 – 0.478	<i>BDL</i> – 61.1	11.3 – 58.9	<i>BDL</i> – 0.274	<i>BDL</i>	13.6 – 15.6	<i>BDL</i> – 1.45	<i>BDL</i> – 1.72	173 – 272	81.3 – 233	<i>BDL</i> – 0.582	805 – 950	<i>BDL</i> – 0.690
10046358	39.1 – 41.0	14.7 – 16.1	0.455 – 0.522	15.6 – 35.7	43.4 – 55.8	<i>BDL</i> – 0.437	<i>BDL</i> – 0.228	14.4 – 16.8	<i>BDL</i> – 2.51	<i>BDL</i> – 7.92	<i>BDL</i> – 517	125 – 148	<i>BDL</i> – 1.52	1,040 – 1,140	<i>BDL</i>
10046359	34.2 – 44.6	12.1 – 15.2	0.363 – 0.492	<i>BDL</i> – 507	54.4 – 103	<i>BDL</i> – 0.289	<i>BDL</i>	12.5 – 17.7	<i>BDL</i> – 0.812	<i>BDL</i> – 8.79	<i>BDL</i> – 763	130 – 245	<i>BDL</i> – 0.966	895 – 1,320	<i>BDL</i> – 0.307
10046360	79.1 – 93.1	12.5 – 12.8	1.76 – 2.14	24.9 – 47.8	199 – 232	0.580 – 1.14	<i>BDL</i> – 0.208	13.6 – 14.7	0.810 – 0.833	5.10 – 7.87	128 – 151	154 – 168	0.915 – 1.31	1,770 – 1,970	0.224 – 0.357
10046361	72.0 – 79.0	14.1 – 14.9	1.56 – 1.84	31.2 – 79.0	218 – 279	0.380 – 0.501	<i>BDL</i>	14.3 – 15.8	<i>BDL</i> – 1.33	4.19 – 10.2	119 – 215	201 – 229	0.819 – 1.33	1,740 – 2,020	<i>BDL</i> – 0.354
10046363	20.3 – 22.9	12.7 – 13.2	0.213 – 0.220	108 – 152	293 – 321	0.161 – 0.253	<i>BDL</i> – 0.287	14.9 – 15.6	0.707 – 0.802	5.84 – 7.62	64.7 – 74.5	251 – 269	0.162 – 0.279	352 – 359	0.136 – 0.453
10046364	41.7 – 71.1	9.20 – 11.3	0.231 – 0.289	<i>BDL</i> – 404	93.0 – 149	<i>BDL</i> – 0.315	<i>BDL</i> – 0.312	12.9 – 17.1	<i>BDL</i> – 0.881	<i>BDL</i> – 7.43	37.1 – 128	398 – 535	<i>BDL</i> – 1.79	375 – 469	<i>BDL</i> – 0.872

Abbreviations: *BDL* = below detection limit; *PCD* = porphyry copper deposit; *No.* = number.